

Hydrodynamically locked morphogenesis in karst and ice flutings

C. Camporeale[†]

Department of Environment, Land and Infrastructure Engineering, Politecnico di Torino,
Corso Duca Abruzzi 24, 10129 Turin, Italy

(Received 16 February 2015; revised 15 May 2015; accepted 26 June 2015;
first published online 30 July 2015)

Two of the most widespread and fascinating patterns observed on cave walls and icefalls – karst and ice flutings – are demonstrated to share the same morphogenesis, whose core is a water film-induced locking mechanism. Creeping flow-based parallel and non-parallel stability analyses are developed through a numerical and analytical approach. These instabilities are shown to develop at inverted overhung conditions. A sharp transition between fluting and ripple-like patterns is presented. The non-parallel problem is solved with the use of Papkovitch–Neuber solutions in order to obtain a finite wavelength selection close to the critical conditions. The method and results can be extended to similar problems where the temporal evolution of the interface is linearly related to the film depth.

Key words: morphological instability, solidification/melting, thin films

1. Introduction

Wavy patterns carved in stone or ice are all-present throughout the Earth's surface. They exhibit an amazing variety of morphological structures, and their beauty and complexity strike everybody. This work deals with a kind of geomorphic pattern that exhibits a relation between environmental fluid mechanics, karst speleothems and ice waterfalls.

It is well known that karst caves, i.e. environments formed from dissolving rocks, contain some of the most astonishing structures such as stalactites, flowstones, draperies and helictites, commonly called speleothems by speleologists (Meakin & Jamtveit 2010). Motivated by their importance as palaeo-climate proxies (Fairchild *et al.* 2006), scientists aim to model the formation of speleothems quantitatively. However, although standard hydrogeochemical processes acting in karst deposits are well known (Kaufmann & Dreybrodt 2007), the morphogenesis of most such water-driven patterns is poorly understood. For instance, the morphological evolution of one of the most emblematic shapes, i.e. stalactites, and the occurrence of regular sub-centimetre ripples on their surface (crenulations; see figure 1*a*) have been modelled only recently (Short *et al.* 2005*a*; Camporeale & Ridolfi 2012*a*). The difficulty in modelling karst morphodynamics is due to the complex interplay between fluid dynamics and geochemistry. Although it is recognized that cave environments are the silent repository of climate records, the dynamics of most of the patterns entrapping these valuable records still lack a comprehensive theory.

[†] Email address for correspondence: carlo.camporeale@polito.it

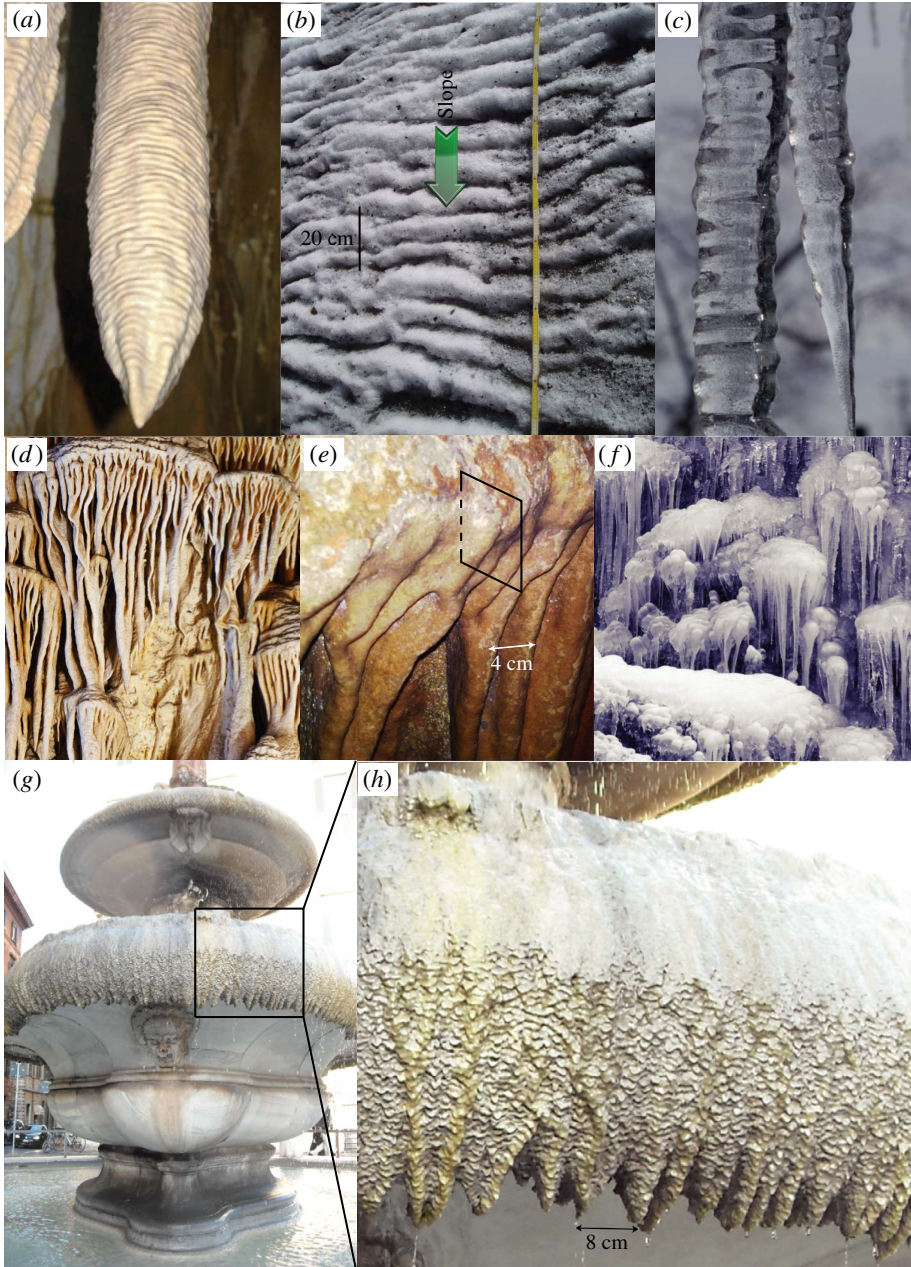


FIGURE 1. (Colour online) (a–c) Examples of karst and ice ripple-like instabilities: (a) crenulations in the Lehman caves, Nevada, USA (<http://www.nps.gov/grba>); (b) ice ripples on the upper surface of the Ciardoney glacier, Italy (Camporeale & Ridolfi 2012b); (c) an example of icicles. (d–h) Examples of karst and ice flutings: (e) longitudinal section of karst fluting head depicted in figure 2; (g,h) appearance of flutings over a calcite concretion on the border of Fountain Ara Coeli (built in 1589, Rome). Also evident is the fine structure of superimposed transverse patterns, ascribable to crenulations.

Unexpectedly, very similar patterns also occur in a completely different environment: icefalls. Unlike the cave environment, where the precipitation–dissolution processes are of geochemical nature, icefall formation is driven by freezing–melting at the phase-change interface. The time scales involved therefore change dramatically with respect to the karst environment: from 10^3 to 10^5 years to a few hours. Typical patterns that evolve on ice are icicles and ice ripples (Ueno *et al.* 2010; Camporeale & Ridolfi 2012*b*). They can be considered the iced counterpart of crenulations, as they are two-dimensional small-scale patterns that develop transversely to the water flow and migrate upstream (figure 1*b,c,f*).

This paper focuses on another kind of elegant pattern, which also develops in these environments, but still awaits explanation: flutings. These structures are widespread in caves and on icefalls and are longitudinally oriented organ-pipe-like formations characterized by regular vertical corrugations, that sometimes hang off slightly concave surfaces (figure 1*d–f*). In karsts, they can also be associated with draperies, also called curtains or ribbons, i.e. weak oscillations in the streamwise direction. While growing downwards over time, flutes may become undulated and coalesce, so changing their transverse wavelength, but the pattern regularity of the upper region is always evident, with a transverse spacing of 2–10 cm. Flutes can emerge from the ceiling of the cave or be preceded by a small zone where water flows on a bulb-shaped surface (dome), at the edge of which flutes detach (figure 1*e*). In icefalls, roughly the same features can be observed: long vertical ice flutes, quite regularly spaced, with transverse wavelengths in fair agreement with karst flutings (figure 1*f*). Differently from icicles or crenulations, flutings have so far never been modelled, although they are widely observed longitudinal patterns.

It is worth noting that longitudinal patterns never occur on the upper part of domes, where only small-wavelength longitudinal wavelets emerge (crenulations or ice ripples). This is also evident simply by observing the border of circular decorative fountains where calcite deposits (figure 1*g,h*). Fluting formation seems therefore to be connected to the flow of a vertical or inverted water film ($\theta > 0^\circ$, according to the representation of figure 2). The main concern of this work is in fact to show that the morphogenesis of both structures is strictly related to hydrodynamics of thin-film flows over an incline. With this aim, two tools are used: a morphological evolution law and film hydrodynamic equations.

Since the seminal work by Nusselt (1916) and Kapitsa & Kapitsa (1949), falling films have become a cornerstone in fluid mechanics. The analysis of surface waves propagating at twice the mean fluid speed were initially addressed through a long-wave approximation (Yih 1963). Subsequent research on falling films at low Reynolds numbers and high slopes faced several issues, ranging from the initial controversy concerning the zero critical Reynolds number at vertical slopes, to the feature of nonlinear dynamics (Sivashinsky & Michelson 1980), solitary waves and subharmonic resonance (Cheng & Chang 1992; Pradas, Tseluiko & Kalliadasis 2011). Most of these issues have been addressed with simplified linear or nonlinear model equations, such as the Benney equation (Benney 1966), the Ginzburg–Landau model, the Kuramoto–Sivashinsky equation and the weighted-residual integral boundary layer (Ruyer-Quil & Manneville 2000). Furthermore, the convective nature of the instability of falling films has been proven numerically (Brevdo *et al.* 1999). Comprehensive reviews of this topic are given in Chang & Demekhin (2002), Craster & Matar (2009) and Kalliadasis *et al.* (2012).

Besides the free surface waves investigated in the above literature, open-channel flows are also subjected to Tollmien–Schlichting waves (also called shear waves)

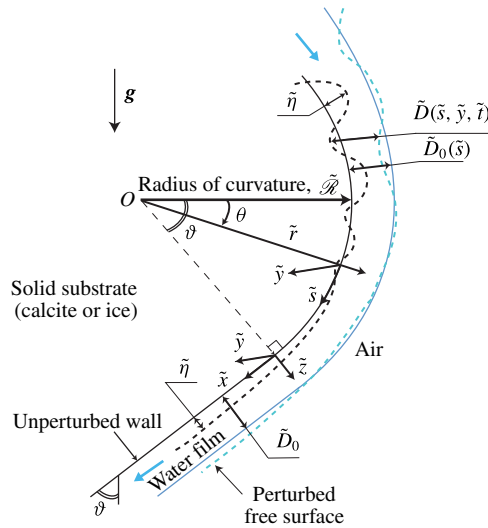


FIGURE 2. (Colour online) Scheme of the longitudinal section marked in figure 1(e). Solid curves: unperturbed conditions. Dashed curves: perturbed conditions.

which propagate at velocities lower than the mean fluid speed (Chu & Dukler 1974). DeBruin (1974) and Floryan, Davis & Kelly (1987) pointed out that the critical Reynolds number of the shear mode is always higher than that of the free surface mode, except for small inclination angles, with the cross-over occurring at very low slopes.

In the current literature, there are very few works where the instability of wavy films is considered with the use of the linearized version of the exact Navier–Stokes equations, namely the Orr–Sommerfeld problem, whose approximate solutions have been provided analytically and numerically (Pierson & Whitaker 1977). Also, most of the works on falling films deal with fixed flat bottoms. The first contribution with undulated topography was made by Wang (1981), but he considered the bottom fixed and the free surface steady. In the same line of research, the progress made on the role of three-dimensional effects (Luo & Pozrikidis 2006) and on the linear resonance of capillary–gravity waves (Wierschem *et al.* 2008) should also be included.

It is worth recalling that all kinds of purely hydrodynamic instabilities (either free surface or Tollmien–Schlichting waves) accounted for by these models are subordinated to a fundamental result in hydrodynamic stability theory, Squire’s theorem: ‘Parallel shear flows first become unstable to two-dimensional perturbations at a value of the Reynolds number that is smaller than any value for which unstable three-dimensional perturbations exist’ (Schmid & Henningson 2001, p. 59). The open-channel version of this theorem therefore ensures that Nusselt’s flat-film base state is more stable to three-dimensional than to two-dimensional disturbances (Yih 1955). However, this is not generally true when the wall is no longer assumed to be a fixed boundary and bottom perturbations are therefore allowed. The occurrence of film-driven flutings suggests that Squire’s theorem in morphodynamic phenomena is inconsistent.

In the context of karst morphodynamics, the coupling between falling film hydrodynamics and speleothem formation has been studied by considering wall-normal

chemical diffusion for several flow conditions and addressing the problem of calcite precipitation under hydrostatic, laminar or turbulent films (Dreybrodt 1988; Dreybrodt & Buhmann 1991). Numerical and experimental analyses have explored wall instabilities at large scales (Hammer *et al.* 2008), calcite terraces have been investigated, both theoretically (Wooding 1991) and numerically (Hammer *et al.* 2008), and mathematical rules for the evolution of stalactites and stalagmites have been developed (Kaufmann 2003; Short *et al.* 2005*a*; Short, Baygents & Goldstein 2005*b*). Additionally, Dressler's depth-averaged equations (Dressler 1978) have also been adopted, with no success in predicting pattern formation (Chan & Goldenfeld 2007). In the context of melting–freezing morphodynamics, the adoption of the Orr–Sommerfeld equation is widespread. When coupled to heat conservation equations and an interface evolution law (i.e. the Stefan condition), this equation allowed the stability analysis of icicles (Ueno *et al.* 2010) and ice ripples (Camporeale & Ridolfi 2012*b*) to be developed theoretically. Some doubts have been raised by Chen & Morris (2013) on the validity of the former theory that we will comment on later, in § 3.4.

It should be noted that none of these modelling approaches have considered the problem of fluting formation in karst or ice environments, and no explanation of the resemblances between forms has yet been given.

In this paper, a unified theory will show that the morphological similarity between karst and ice flutings is not accidental. With this in mind, the concept of hydrodynamically locked morphogenesis (HLM) is introduced. In HLM the free surface dynamics triggers longitudinal pattern formation at the liquid–solid interface. The primary linear instability is hydrodynamic in nature, with the instability initiated by the free surface coupled to the fluid momentum. As this instability saturates due to nonlinear effects to a bounded nonlinear state, the resulting solution drives the longitudinal patterns found at the liquid–solid interface. HLM is due to the physics of inverted flows and it is substantially different from what occurs in other ripple-like patterns, such as icicles and crenulations, where chemical and thermal mechanisms are crucial to the wavelength selection. According to the ‘HLM conjecture’, a purely fixed-wall hydrodynamic theory selects the same patterns as the complete morphodynamic one. Analytical results provided by film-flow stability analysis can therefore be used to model fluting morphogenesis.

This paper is organized as follows. In the next section (§ 2), a formal derivation of a morphological evolution equation is provided and the mathematical problem is formulated for both environments. Section 3 provides some analytical and numerical results when non-parallelism and wall curvature are neglected, in order to illustrate some phenomenological results. The fluting–ripple transition is also discussed and the validity of the HLM conjecture is justified. In § 4, an approximate solution of the non-parallel theory is provided, and finite wavelength selection is obtained in a neighbourhood of the vertical tangent point. In § 5, the physical mechanisms underlying the HLM are illustrated and a potential consequence in palaeo-flow reconstruction arising from the match between the parallel and non-parallel theory is discussed. Finally, some conclusions are drawn in § 6.

2. Formulation

Let us consider a pendent film which flows along the underside of a wall. For the sake of simplicity, the domain is separated into two parts: a curved and a flat region. The upstream curved region is assumed to have a cylindrical shape,

with centre of curvature O and constant radius of curvature $\tilde{\mathcal{R}}$, and it is joined to the flat region downstream (see figure 2). In the curved region, we will adopt a cylindrical reference frame $\{\theta, \tilde{r}, \tilde{y}\}$, corresponding to the azimuthal, radial and spanwise coordinates, respectively. Note that the curvilinear coordinate is $\tilde{s} = \tilde{\mathcal{R}}\theta$, so the alternative reference frame $\{\tilde{s}, \tilde{r}, \tilde{y}\}$ will also be adopted in the following. In the flat region, we will use the standard Cartesian reference frame $\{\tilde{x}, \tilde{y}, \tilde{z}\}$, corresponding to the streamwise, spanwise and wall-normal coordinates, respectively. In this latter region, the slope of the wall with respect to the vertical axis reduces to a constant value, i.e. $\theta \rightarrow \vartheta$ (see figure 2) and, for unperturbed conditions, the depth and the surface velocity are respectively provided by Nusselt's solutions

$$\tilde{D}_0 = \left(\frac{2\nu^2 Re}{g \cos \vartheta} \right)^{1/3}, \quad \tilde{U}_0 = \left(\frac{g \cos \vartheta Re^2 \nu}{2} \right)^{1/3}, \quad (2.1a,b)$$

where g is the gravitational acceleration, ν is the viscosity and $Re = \tilde{U}_0 \tilde{D}_0 / \nu$ is the Reynolds number. Henceforth, tilde refers to the dimensional notation.

In order to tackle the morphological instability, a wall evolution equation is necessary. With this aim, it is convenient to focus on the flat region and to decompose the film thickness into the sum of the Nusselt depth, \tilde{D}_0 , and a (small) local pattern-induced perturbation, $\epsilon \tilde{d}(\tilde{x}, \tilde{y}, \tilde{t})$. The quantity ϵ is a small perturbative parameter that represents the amplitude of the perturbation, so \tilde{d} is of order one. At length scales much larger than a single crystal, it can be shown that the growth rate of both calcite–water and ice–water interfaces is linearly related to the depth perturbation $\epsilon \tilde{d}$.

Let us first consider the karst environments. In the work by Short *et al.* (2005a), the stalactite shape was derived by demonstrating that the calcite deposition rate can be written as

$$\varrho \frac{d\tilde{\eta}}{d\tilde{t}} = a \{ \tilde{D}_0 + \epsilon \tilde{d}(\tilde{x}, \tilde{y}, \tilde{t}) \} \{ k'_- [\text{Ca}^{2+}] - k_+ H [\text{CO}_2]_\infty + k_0 [\text{H}^+] \}, \quad (2.2)$$

where ϱ is the ratio of molar mass to density for calcite, $\tilde{\eta}$ is the wall perturbation, square brackets refers to ion concentration, H is Henry's constant, k'_- , k_+ and k_0 are pH-dependent reaction constants, and the subscript of the carbon dioxide concentration refers to far atmospheric values. The coefficient a accounts for geometrical effects but is very close to unity for thin films, so it can be omitted in the present context (as also remarked by Short *et al.* (2005b)). The term related to calcium concentration is formally space-dependent; however, as already pointed by Short *et al.* (2005a), the calcium concentration profile is nearly flat, because of the very low deposition rate, so there is no significant reduction of calcium along the length of the speleothem. On the other hand, if one were interested in modelling sub-centimetre transverse ripples (i.e. crenulations), it would be important to consider calcium concentration as harmonically perturbed in the streamwise direction, as pointed out by Camporeale & Ridolfi (2012a). For our purposes, the whole content of the second curly brackets – which we denote $\varrho \mathcal{F}_K$ – can be considered instead independent of hydrodynamics. In this way, (2.2) can be rewritten in the generalized form of an evolution equation,

$$\frac{\partial \tilde{\eta}}{\partial \tilde{t}} = A + \epsilon B \tilde{d}, \quad (2.3)$$

where $A = \mathcal{F}_K \tilde{D}_0$ and $B = \mathcal{F}_K$.

In the ice context, the master equation for wall evolution is instead the celebrated Stefan equation, which states the heat balance at a freezing–melting interface and reads

$$\rho_i \mathcal{L} \frac{d\tilde{\eta}}{dt} = [(\kappa_i \nabla \tilde{T}_i)_{I^-} - (\kappa_w \nabla \tilde{T}_w)_{I^+}] \cdot \mathbf{n}_I, \tag{2.4}$$

where $\kappa_{w,i}$ are the thermal conductivity of water and ice, respectively, ρ_i is ice density, \mathcal{L} is the latent heat, \mathbf{n}_I is the normal versor to the liquid–solid interface, and $\tilde{T}_{w,i}$ are respectively water and ice temperature. Similarly to the depth, these latter can be decomposed into the sum of a base state plus a pattern-induced perturbation, namely $\tilde{T}_{w,i} = \tilde{T}_{0,w,i}(\tilde{z}) + \epsilon \tilde{\Theta}_{w,i}(\tilde{x}, \tilde{y}, \tilde{z})$. Additionally, we can introduce the normalized vertical coordinates $\zeta = (\tilde{z} - \tilde{\eta})/\tilde{D}$ and $\zeta_i = (\tilde{z} - \tilde{\eta})/\tilde{S}$, where \tilde{S} is an assigned depth in the ice. In this way the liquid and the solid domains are rectangularized so that $\zeta \in [0, 1]$ and $\zeta_i \in [-1, 0]$, respectively. One therefore obtains that $\tilde{T}_{0,w,i}$ are linearly distributed over the film depth, i.e.

$$\tilde{T}_{0,w} = \tilde{T}_S \zeta, \quad \tilde{T}_{0,i} = \tilde{T}_b \zeta_i, \tag{2.5a,b}$$

where \tilde{T}_S is a prescribed free surface temperature (in equilibrium with air), and \tilde{T}_b is the ice temperature at $\tilde{z} = -\tilde{S}$ (i.e. $\zeta_i = -1$). Since the Prandtl number of water at melting conditions is equal to $Pr = 13$ and Re can be assumed to be of order 10^{-2} or less, the Péclet number, $Pe = Pr Re$, is $O(10^{-1})$ or less. This justifies the neglect of thermal convection in the heat equation of the liquid phase. The perturbations $\tilde{\Theta}_w$ and $\tilde{\Theta}_i$ therefore satisfy the Laplace equations $\nabla^2 \tilde{\Theta}_{w,i} = 0$, with homogeneous boundary conditions that ensure the melting temperature at the liquid–solid interface and the constancy of the overall heat flux throughout the domain (i.e. the heat flux induced by perturbations is zero). With the use of the normalized coordinates, after linearizing with respect to ϵ and Fourier-transforming from $\{\tilde{x}, \tilde{y}\}$ to the horizontal wavevector $\tilde{\mathbf{k}} \equiv \{\tilde{\alpha}, \tilde{\beta}\}$, where $\tilde{\alpha}$ is the streamwise wavenumber and $\tilde{\beta}$ is the spanwise wavenumber, the diffusive thermal problem becomes

$$\left[\frac{d^2}{d\zeta^2} - \tilde{D}_0^2 \tilde{k}^2 \right] \tilde{\Theta}_w^* + \tilde{D}_0 \tilde{k}^2 \tilde{T}_s (\tilde{D}_0 + \tilde{d}^* \zeta) = 0, \tag{2.6}$$

$$\left[\frac{d^2}{d\zeta_s^2} - \tilde{S}_0^2 \tilde{k}^2 \right] \tilde{\Theta}_i^* + \tilde{S}_0 \tilde{D}_0 \tilde{k}^2 \tilde{T}_b (1 + \zeta_s) = 0, \tag{2.7}$$

$$\tilde{\Theta}_w^*(0) = \tilde{\Theta}_i^*(0) = \left. \frac{d\tilde{\Theta}_w^*}{d\zeta} \right|_{\zeta=1} = \left. \frac{d\tilde{\Theta}_i^*}{d\zeta} \right|_{\zeta=-1} = 0. \tag{2.8}$$

The asterisk refers to the Fourier transform while $\tilde{S}_0 = \tilde{S} - \epsilon$ and $\tilde{k} = |\tilde{\mathbf{k}}|$. The solutions of (2.6)–(2.8), when used in (2.4), at the first order in ϵ , provide

$$\rho_i \mathcal{L} \frac{d\tilde{\eta}^*}{dt} = -\frac{\mathcal{F}_I}{\tilde{D}_0} + \epsilon \left\{ \frac{\mathcal{F}_I}{\tilde{D}_0} \tilde{d}^* - \frac{\tilde{k}^2}{2} [(2\tilde{D}_0 + \tilde{d}^*)\kappa_w \tilde{T}_s - \tilde{S}_0 \kappa_i \tilde{T}_b] \right\} + O(\epsilon^2), \tag{2.9}$$

where $\mathcal{F}_I = \kappa_w \tilde{T}_s + \kappa_i \tilde{T}_b$. At this point, it is instructive to perform an order-of-magnitude analysis of (2.9). The flow conditions considered herein imply that \tilde{D}_0 varies in the range $[10\text{--}50] \mu\text{m}$ (see also table 1), while the morphological patterns we are considering have centimetre length scale, namely $\tilde{k}^2 \sim 10^{-7} \mu\text{m}^{-2}$. Since by

\tilde{D}_0 (μm)	\tilde{U}_0 (mm s^{-1})	\tilde{c} (cm century^{-1})	\tilde{l}_c (mm)	\tilde{T} ($^\circ\text{C}$)	\tilde{T}_s ($^\circ\text{C}$)	\tilde{T}_b ($^\circ\text{C}$)	
10–50	0.02–10	5–40	2.7–2.77	0–30	0.01–0.1	–0.01	
Re	Pe	Ka	Ma	γ_i	γ_k	k	ϑ (rad)
10^{-3} – 10^{-1}	10^{-2} –1	1740–3194	0.3–0.6	10 – 10^4	10^5 – 10^9	0–1	0 – $\pi/2$

TABLE 1. Typical values of dimensional and dimensionless quantities.

definition $\tilde{d} = O(1)$ and \tilde{S}_0 has the same order of magnitude as \tilde{D}_0 , it is evident that the second term in the curly brackets is much smaller than the first one. The back-transform of the resulting approximate equation falls again into the form of (2.3), provided the following hold:

$$A = -\frac{\mathcal{F}_I}{\rho_i \mathcal{L} \tilde{D}_0}, \quad B = \frac{\mathcal{F}_I}{\rho_i \mathcal{L} \tilde{D}_0^2}. \tag{2.10a,b}$$

We note that, depending on the signs of the terms \mathcal{F}_K and \mathcal{F}_I , both karst and ice environments can be modelled as either depositional or dissolutive (remember that \tilde{T}_{0_i} is in fact negative by construction). However, considering the formative conditions of the morphological patterns that superimpose over the net evolution of the liquid–solid substrate, it is reasonable that karst flutings occur in the same conditions that have generated the supporting speleothem, i.e. a depositional environment. On the contrary, the presence of a melt flow during ice fluting morphogenesis suggests that, in the absence of other water sources, the icefall is melting. Based on such considerations and without any loss of generality, we will assume henceforth that \mathcal{F}_K and \mathcal{F}_I are both positive quantities.

At this point, all lengths and velocities can be made dimensionless by using the Nusselt solutions (2.1a,b), respectively, and the dimensionless time follows accordingly as $t = \tilde{t} \tilde{U}_0 / \tilde{D}_0$. Quantities without a tilde are therefore intended to be dimensionless. The evolution equation (2.3) recast in general dimensionless form is

$$\gamma \frac{d\eta}{dt} = \pm 1 + \epsilon d(\tilde{x}, \tilde{y}, t), \tag{2.11}$$

where the positive (negative) sign refers to the karst (ice) case and $\gamma = \tilde{U}_0 / B \tilde{D}_0$ is the ratio of the morphological to hydrodynamic time scales. In this unified approach, γ is the only element that discriminates between the karst and ice problem, henceforth referred to with subscripts K and I , respectively. Assuming $\tilde{T}_s = 0.1^\circ\text{C}$, $\tilde{T}_b = -0.01^\circ\text{C}$ and standard conditions for speleothem formation, i.e. $d\tilde{\eta}_K/dt = \tilde{c} \sim O(\text{cm century}^{-1})$ (e.g. Short *et al.* 2005b), one obtains

$$\gamma_I = 10^4 Re, \quad \gamma_K = \frac{\tilde{U}_0}{\tilde{c}}, \tag{2.12a,b}$$

which furnish γ_I of order 10^2 and γ_K of order 10^7 or larger (see table 1 for a summary of typical values of dimensional and dimensionless quantities). Without any loss of generality, the validity of (2.11) can also be extended to the curved region, provided the function d is set to depend on (θ, y, t) .

The high values of the ratio between the morphological and hydrodynamic time scales, γ , allows one to adopt the so-called quasi-steady approximation, where the flow field \mathbf{u} is assumed to be slaved to the domain deformation induced by changes in either η or D . This assumption is customary in morphodynamic problems (Camporeale & Ridolfi 2012b) and allows us to neglect the time derivative in momentum equations. The main modelling effect of this approximation is to disregard shear waves (Tollmien–Schlichting waves), which are always stable for the conditions herein considered ($\theta > 0$ and $Re \ll 1$).

Bearing in mind the above remarks, the governing equations are the dimensionless form of Navier–Stokes equations for incompressible fluids (Kalliadasis *et al.* 2012)

$$\mathbf{u} \cdot \nabla \mathbf{u} + \nabla p = \frac{1}{Re} \nabla^2 \mathbf{u} + \mathbf{F}, \tag{2.13}$$

$$\nabla \cdot \mathbf{u} = 0, \tag{2.14}$$

where $\mathbf{F} = (g\tilde{D}_0/\tilde{U}_0^2)\{\sin\theta, 0, \cos\theta\}$ accounts for gravitational effects. The liquid–solid interface is a dynamic surface that is defined by $\mathcal{S}(x, y, t) \equiv z - \eta(x, y, t) = 0$. Similarly, the free surface is indicated through $\mathcal{F}(x, y, t) \equiv z - \eta(x, y, t) - D(x, y, t) = 0$. It follows that the boundary conditions read

$$\frac{D\mathcal{S}}{Dt} = 0, \tag{2.15}$$

$$\frac{D\mathcal{S}}{Dt} = \begin{cases} 0 & \text{(dissolution–precipitation),} \\ \rho_{iw} \frac{\partial \eta}{\partial t} & \text{(melting–freezing),} \end{cases} \tag{2.16}$$

$$(\mathbf{n} \cdot \mathbf{T} \cdot \mathbf{t})_{z=\eta+D} = 0, \quad (\mathbf{n} \cdot \mathbf{T} \cdot \mathbf{n})_{z=D} + Ka \left(\frac{2}{Re^5 \cos^2 \theta} \right)^{1/3} \mathcal{H}_{\mathcal{S}} = 0, \quad (\mathbf{t} \cdot \mathbf{u})_{z=\eta} = 0, \tag{2.17a–c}$$

where $D/Dt = \partial/\partial t + \mathbf{u} \cdot \nabla$ is the material derivative, p is pressure, ρ_{iw} is the density ratio of ice to water, \mathbf{n} and \mathbf{t} are the unit normal and tangent vector to a generic surface, respectively, $\mathbf{T} = p\mathbf{I} - 2Re^{-1}\mathbf{D}$ is the dimensionless Newtonian stress tensor (with \mathbf{I} and \mathbf{D} the identity matrix and the rate-of-strain tensor, respectively) and $\mathcal{H}_{\mathcal{S}} = \{[(\mathbf{I} - \mathbf{n}_S \mathbf{n}_S) \cdot \nabla] \cdot \mathbf{n}_S\}/2$ is the local mean curvature of the free surface (while $\mathcal{H}_{\mathcal{F}}$ is the corresponding value at the interface). The parameter $Ka = l_c^2 g^{2/3} \nu^{-4/3}$ is the so-called Kapitza number (Chang & Demekhin 2002), representing the ratio between surface tension and viscous forces, which depends on fluid properties ($l_c \sim 2\text{--}3$ mm is the water capillary length). Henceforth, if not further specified, we will assume the melting conditions for the ice and standard conditions, $T = 20^\circ\text{C}$, for karsts. It is also worth noting that thermocapillary effects can be neglected, since the Marangoni number $Ma = Ka\delta_\sigma$ is very small, where $\delta_\sigma \sim 1.8 \times 10^{-4}$ is the temperature-induced (relative) variation in the surface tension (see table 1 and also refer to Kalliadasis *et al.* (2012, par. 9.5.3)). Since calcium concentration does not affect surface tension, solutal capillarity is also negligible.

Equation (2.15) is the kinematic condition for the free surface (responsible for surface waves), while equations (2.16) are the kinematic condition for the liquid–solid interface, where the source term on the right-hand side that appears in the melting–freezing case accounts for the meltwater flux entering the film (Hutter 1983, p. 136). Equations (2.17a,b) state the tangential and normal components of momentum conservation at the free surface, i.e. the so-called dynamic conditions. We emphasize that the last term in (2.17b) takes into account the effect of surface tension. Equation (2.17c) states the no-slip condition. In summary, the complete dimensionless mathematical problem is provided by (2.11) and (2.13)–(2.17).

3. Parallel stability theory

As a first step, we neglect the curvature of the wall and perform a stability analysis in the planar region of the wall depicted in figure 2. As already done in the thermal problem, Prandtl’s mapping $z = \eta + \zeta(1 + d)$ is also adopted in the fluid dynamics problem, and a normal mode perturbation is assumed by following the decomposition of film thickness already introduced in the previous section, with the ansatz

$$\{\eta, D\} = \left\{ \pm \frac{t}{\gamma}, 1 \right\} + \epsilon \hat{d} \left\{ \frac{1}{\gamma}, 1 \right\} e^{\lambda t + i(\alpha x + \beta y)} + \text{c.c.}, \tag{3.1}$$

where $i = \sqrt{-1}$, λ is the complex growth factor and the hat refers to the perturbation mode. As will be evident in the sequel, the time dependence of the base state of η has no effects on the equations governing the perturbations, since it is linear in time and can be virtually eliminated by a rigid wall-normal translation of the reference frame ($\zeta \rightarrow \zeta \pm t/\gamma$).

3.1. The morphodynamic Orr–Sommerfeld model

From standard arguments (Chang & Demekhin 2002), it is well known that the linearized form of the problem (2.13)–(2.17) is equivalent to the Orr–Sommerfeld problem extended to open boundary domains. Accordingly, let us set $k^2 = |\mathbf{k}|^2 = \alpha^2 + \beta^2$, where α and β are the streamwise and spanwise components of the wavevector, respectively, and define a suitable streamfunction $\phi = \phi_0(\zeta) + \hat{\phi}(\zeta) \exp[\lambda t + i(\alpha x + \beta y)]$. The constraint of the continuity equation allows the velocity perturbation modes $\{\hat{u}, \hat{v}, \hat{w}\}$ to follow the relations (Camporeale & Ridolfi 2012b)

$$\alpha \hat{u} + \beta \hat{v} = k \frac{d\hat{\phi}}{d\zeta} + \alpha(1 + \hat{d})u_0(\zeta), \quad \hat{w} = -ik\hat{\phi}, \tag{3.2a,b}$$

where $u_0 = d\phi_0/d\zeta = 2\zeta - \zeta^2$ is the base-state Nusselt velocity profile. The final linearized set of equations reads

$$\left(\frac{d^4}{d\zeta^4} - 2k^2 \frac{d^2}{d\zeta^2} + k^4 \right) \hat{\phi} = i\alpha Re \left[u_0 \left(\frac{d^2}{d\zeta^2} - k^2 \right) + 2 \right] \hat{\phi}, \tag{3.3}$$

$$k\hat{\phi} - i\chi\gamma^{-1}\hat{d} = 0, \quad k \frac{d\hat{\phi}}{d\zeta} + 2\alpha = 0 \quad (\zeta = 0), \tag{3.4a,b}$$

$$\left(k \frac{d^2}{d\zeta^2} + k^3 \right) \hat{\phi} - 2\alpha(1 + \hat{d}) = 0 \quad (\zeta = 1), \tag{3.5}$$

$$\frac{d}{d\zeta} \left(\frac{d^2}{d\zeta^2} - 3k^2 - i\alpha Re \right) \hat{\phi} - \Omega(1 + \hat{d}) = \lambda Re \frac{d\hat{\phi}}{d\zeta} \quad (\zeta = 1), \tag{3.6}$$

$$(i\lambda - \alpha)(1 + \hat{d}) = k\hat{\phi} \quad (\zeta = 1), \tag{3.7}$$

$$\gamma\lambda = \hat{d}, \tag{3.8}$$

where $\Omega = ik[Ka(2/Re^2 \cos \vartheta)^{1/3}k^2 - 2 \tan \vartheta]$ and $\chi = 1 - \rho_i/\rho_w$ in the I case and $\chi = 1$ in the K case. Note that the quantity Ω is the sum of a term proportional to the Kapitza number, accounting for capillarity effects, and one accounting for gravitational effects, which are competing mechanisms for the stability problem, as will be shown in the Discussion. Additionally, in order to obtain (3.4), we have substituted (3.8) in the kinematic equation at the wall. In the following, the set of equations (3.3)–(3.8) will be referred as the ‘morphodynamic Orr–Sommerfeld’ (MOS) model.

3.2. Numerical solution

The MOS model (3.3)–(3.8) is solved numerically through a spectral Galerkin technique by adapting the procedure developed in Camporeale, Canuto & Ridolfi (2012) and Camporeale & Ridolfi (2012*b*), to which the reader is referred for additional details. Although analytical results will be provided in the following, a consistent numerical solution is in fact decisive in order to distinguish the exact boundaries for pattern formation parametrically.

Essentially, the differential system can be recast into a generalized algebraic eigenvalue problem of the form $\mathcal{S}\{\phi_i\} = \lambda_i \mathcal{M}$ with \mathcal{M} and \mathcal{S} as the mass and stiffness matrices, respectively. With this in mind, a modal representation of the solution is adopted, where the function $\hat{\phi}$ is expanded in the (truncated) spectral form

$$\hat{\phi} = \sum_{i=-3}^N \phi_i \Phi_i(\xi), \tag{3.9}$$

with Φ_i being a set of trial functions, whereas ϕ_i and \hat{d} represent the new unknowns. For numerical convenience, the vertical coordinate is further mapped into the range $\xi \in [-1, 1]$, according to $\xi = 2\zeta - 1$. The original ordinary differential equation problem is multiplied by a set of (smooth) test functions with zero first derivative at $\xi = \pm 1$ and zero value at $\xi = -1$ and integrated over the domain $[-1, 1]$. The repeated use of integration by parts allows the fourth derivative in (3.3) to be reduced to a second-order derivative; in addition, the dynamic boundary condition (3.6) is incorporated in the mass and stiffness operators in the so-called weak form, through the boundary term that arises from the integration by parts. The correct choice of the trial and test functions enables the use of the remaining boundary conditions to be set in a strong form, that is, as additional rows in the ultimate algebraic system.

We consider the set of polynomials

$$\Phi_i = \sqrt{i + \frac{3}{2}} \left(\frac{L_{i+3} - L_{i+1}}{(2i + 3)(2i + 5)} - \frac{L_{i+1} - L_{i-1}}{(2i + 1)(2i + 3)} \right), \quad i \in [1, N - 3], \tag{3.10}$$

where $L_i(\xi)$ denotes the i th Legendre polynomial. These functions are obtained by integrating twice each Legendre polynomial, while enforcing zero boundary conditions at $\xi = \pm 1$ for the function and its first derivative. The set of functions in (3.10) completes the set of solutions of the classical Orr–Sommerfeld problem, where the boundary conditions are all homogeneous (e.g. Shen 1994). In order to accommodate non-vanishing boundary conditions, we need to add further low-degree polynomials, which are

$$\Phi_{-3} = \frac{1}{4}(\xi + 1)^2(\xi - 1), \quad \Phi_{-2} = \frac{1}{4}(3 - \xi^2 - 2\xi), \tag{3.11a,b}$$

$$\Phi_{-1} = \frac{1}{2}(1 - \xi^2), \quad \Phi_0 = \frac{1}{4}(3 + 2\xi - \xi^2). \tag{3.12a,b}$$

It is straightforward to verify that trial and test spaces for the present problem are arranged in the following way, respectively,

$$\Phi_i = \{\Phi_{-3}, \Phi_{-2}, \Phi_{-1}, \Phi_0, \Phi_i\}^T, \quad V = \{\Phi_0, \Phi_i\}^T. \tag{3.13a,b}$$

The trial functions Φ_{-3} and Φ_{-2} become unnecessary in the particular cases $\gamma \rightarrow \infty$ and $\alpha = 0$, respectively, being the homogeneous boundary conditions at the wall.

The above specifications allow one to obtain the mass and stiffness matrices (not reported for the sake of the space). The adoption of a Galerkin discretization

with the aforementioned Legendre modal basis and the use of integration by parts reduces the numerical complexity due to the fourth- and third-order derivatives of the Orr–Sommerfeld–Squire problem. This trick eliminates pointwise values of the higher derivative in the weak form of the equations, thus increasing the accuracy of the results, and avoids the occurrence of spurious eigenvalues. Unlike the classical Orr–Sommerfeld problem, the quasi-steady approximation yields a void mass matrix, except for three lines corresponding to non-homogeneous equations (3.6)–(3.8). The eigenvalue problem is therefore reduced to the solution of a 3×3 linear system.

3.3. The Stokes model: analytical solution

In the context of the Stokes regime ($Re \ll 1$), the right-hand sides of (3.3) and (3.6) can be neglected. This choice is numerically justified by the fact that the range of unstable wavenumbers and the considered Reynolds numbers yield the term αRe to be less than 10^{-3} . Furthermore, from (3.8), it follows that $\lambda Re = O(\gamma^{-1} Re)$, which is $<10^{-3}$ for the ice case and $<10^{-8}$ for the karst case. We also recall that dropping the right-hand side of (3.3) provides a biharmonic equation that is exact on the β -axis, while the asymptotic case $\gamma \rightarrow \infty$ provides the classical Orr–Sommerfeld problem with no wall evolution. In summary, an analytical approach encompassing two fundamental approximations will be considered: neglecting convective terms in the momentum equation and the right-hand side of (3.6).

The thus derived differential Stokes problem allows a straightforward but cumbersome explicit solution for $\hat{\phi}(1)$, as a function of the unknown \hat{d} and parameters α , k , Re and ϑ . By substituting the expression for $\hat{\phi}(1)$ in the linearized kinematic condition (3.7), and combining with the wall evolution equation (3.8), we obtain a quadratic characteristic polynomial for λ , with two analytical solutions:

$$\lambda_{\pm} = -\sigma_1 \pm (\sigma_1^2 - 2\sigma_2)^{1/2}, \tag{3.14}$$

where

$$\begin{aligned} \sigma_1 = & \frac{i\alpha}{2} + \frac{1}{2\gamma} - \frac{k \cosh k + \sinh k (2ik^2 - R\alpha)}{k\gamma (2k^2 + \cosh(2k) + i\alpha Re + 1)} \\ & + \frac{2k^3\Omega - k^2\Omega \sinh(2k) + i\alpha (4k^4 + i(2k^2 + 1)\alpha Re) - i\alpha^2 Re \cosh(2k)}{4k^4 (2k^2 + \cosh(2k) + i\alpha Re + 1)}, \end{aligned} \tag{3.15}$$

$$\begin{aligned} \sigma_2 = & \frac{i\alpha}{2\gamma} - \frac{2k^3\Omega - 2k^2 \cosh k (4k^2\alpha + \Omega \sinh k + 2i\alpha^2 Re)}{4i\gamma k^4 (2k^2 + \cosh(2k) + i\alpha Re + 1)} \\ & + \frac{\alpha (4k^4 + i\alpha Re + 2ik^2) - i\alpha^2 Re(\cosh(2k) - 4k \sinh k)}{4i\gamma k^4 (2k^2 + \cosh(2k) + iR\alpha + 1)}. \end{aligned} \tag{3.16}$$

The values of $\lambda_{\pm}^{(r)} \equiv \text{Re}[\lambda_{\pm}]$ provide two modes of the growth rate of the perturbations that are related to the wall and free surface dynamics. The feature of the Stokes solution will be compared to the numerical solution of the MOS problem in the following section.

The critical condition on the β -axis is obtained by setting $\alpha = \sigma_2 = 0$, leading to

$$\beta_c = (2Re \sec \vartheta)^{1/3} \sqrt{\frac{\sin \vartheta}{Ka}}. \tag{3.17}$$

The square root in the above formula shows that fluted perturbations are stable when $\vartheta < 0$ and this condition does not depend on the parameter γ . Thus, the unstable domain on the β -axis is not affected by the wall evolution dynamics, which is a first clue of HLM, as will be explained in the sequel. A synthetic result is provided by writing (3.17) in terms of the critical wavelength $L_c = 2\pi\tilde{D}_0/\beta_c$. Quite curiously, this quantity does not depend on Re and can be written in the compact form as $L_c/l_c = 2\pi\sqrt{\csc \vartheta}$.

3.4. Results

The above mathematical model involves four dimensionless numbers (Re , α , β , ϑ) plus the calcite depositional rate, c , which is given in cm century^{-1} for the sake of clarity. An extensive exploration of the results in the parameter subspace $\{Re, \alpha, \beta, |\vartheta|, c\} < \{1, 1, 1, \pi/2, 40\}$ demonstrates that the real part of the least stable eigenvalue (henceforth referred to as $\lambda^{(r)}$) is positive under the condition $\vartheta > 0$ only. The theory therefore provides instability only in inverted conditions, in agreement with observations (e.g. figure 1). This result has been obtained through both the numerical and analytical solution and for the karst and ice cases.

However, some important differences have emerged between the analytical and numerical solutions, which are worth remarking upon. Firstly, the (approximate) analytical solution localizes the maximum growth rate on the β -axis systematically, which means that Squire's theorem is always violated at any Re . Conversely, the numerical solution is able to distinguish between two patterns: fluting and ripple. In the former case, the maximum growth rate is on the β -axis; in the latter case, it is on the α -axis. If we define the function $Re_t(\vartheta; \gamma)$ as the slope-dependent value of the Reynolds number for the transition between these two modes, then fluting is dominant at $Re < Re_t$, while ripples dominate at $Re > Re_t$. The shift between these two modes is sharp, that is, there is no hybrid bulb-like patterns with α and β both not null. As stated earlier, the analytical solution is only valid in the fluting regime, which is also the focus of the present work.

The above remarks are well summarized in figure 3(a) where, for the K case, we observe that the fluting regime extends to higher values of Re with increase in the calcite deposition rate, c , and the transition curve has a maximum at $\vartheta = [1-10]^\circ$ and $Re = O(10^{-2})$. In the I case (figure 3b), the transition occurs at $Re = O(1)$. This remarkable difference between the ice and karst cases is confirmed by the substantial absence of ripple-like rings on ice stalactites of icefalls when the Reynolds number is low.

It is also instructive to discuss a few particular cases. Figure 4(a) shows the numerically computed contour map of $\lambda^{(r)}$ in the α - β plane for the particular case A_K , marked in figure 3(a) (K case, $Re = 0.0115$, $\vartheta = 2^\circ$, $\gamma = 5.4 \times 10^7$). The outer contour line refers to the critical condition, namely $\lambda^{(r)} = 0$ (dark blue curve). According to (3.17) the theoretical value of β_c is 9×10^{-4} , which is in perfect agreement with the intercept of the outer contour with the β -axis. Since this case belongs to the fluting regime, the maximum growth rate occurs at $\alpha = 0$. There is in fact a very narrow internal boundary layer with high numerical values reported on the β -axis. A close-up of this thin layer is reported in figure 4(b) by using the analytical solution (3.14)–(3.16). The numerical solver described in § 3.2 provides an almost identical plot (not reported), supporting the fact that, very close to the β -axis (α being of order 10^{-8} or less in this case), the Stokes approximation theory provides reliable results. *A posteriori*, it is thus evident that the occurrence of such a strange

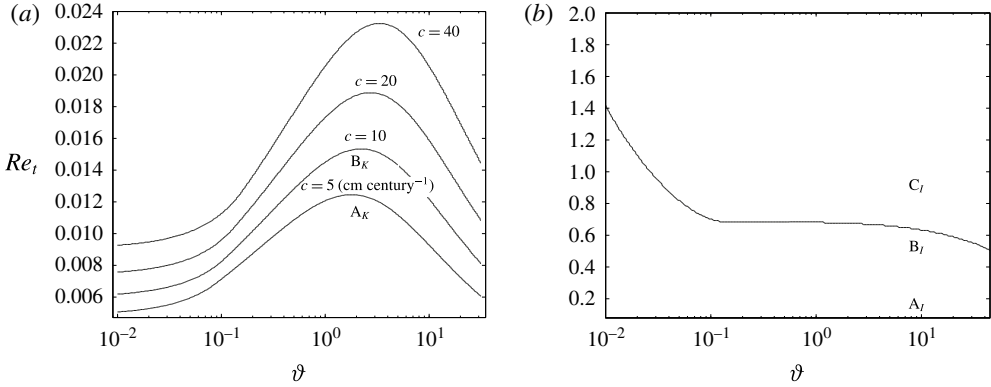


FIGURE 3. Boundaries between fluting ($Re < Re_t$) and ripple ($Re > Re_t$) regimes as a function of ϑ : (a) karst case at different calcite deposition rates; (b) ice case. Points A, B and C refer to some particular cases that are commented upon in the text.

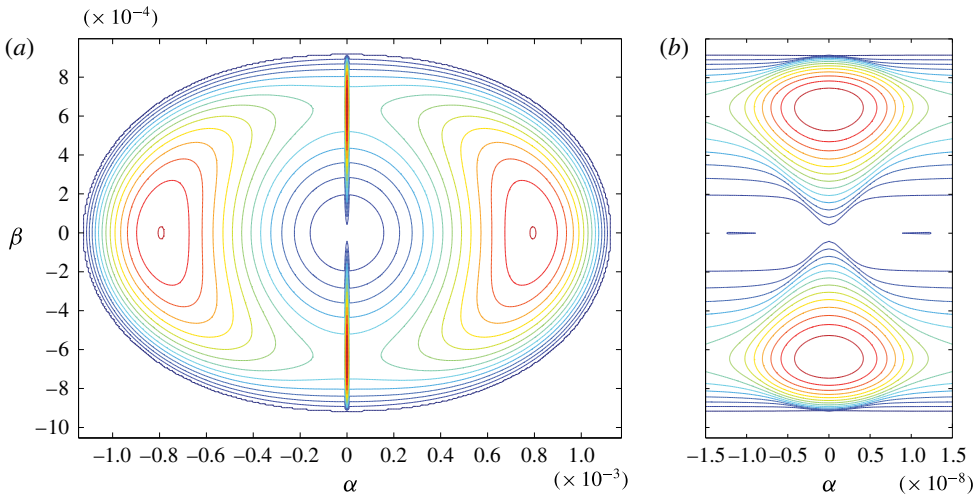


FIGURE 4. (Colour online) (a) Contour plot of $\lambda^{(r)}$ from blue to red, for the case A_K (maximum = 1.2×10^{-8}). (b) Close-up of a thin stripe around the β -axis (numerical and analytical computations provide identical plots).

narrow boundary layer – which is crucial for the existence of the fluting regime – is not a numerical artifact, since it is confirmed by the Stokes approximation theory. This theory is in fact exact on the β -axis (see § 3.3). Incidentally, we note that the width of this layer scales as γ^{-1} .

Furthermore, far from the β -axis, but on the α -axis, two other relative maxima are also located. In the case of the fluting (ripple) regime, these maxima are lower (higher) than the peaks on the β -axis. Differently from the β -axis, these additional structures are not correctly provided by the the Stokes approximation theory, regardless of the Reynolds number, and therefore the ripple regime is not detectable analytically. This latter finding is much more evident if the behaviours on the α - and β -axes are directly compared against the growth rate (see figure 5). In the fluting regime (case A_K , panel a), the maximum along the β -axis (thick solid line) is larger than

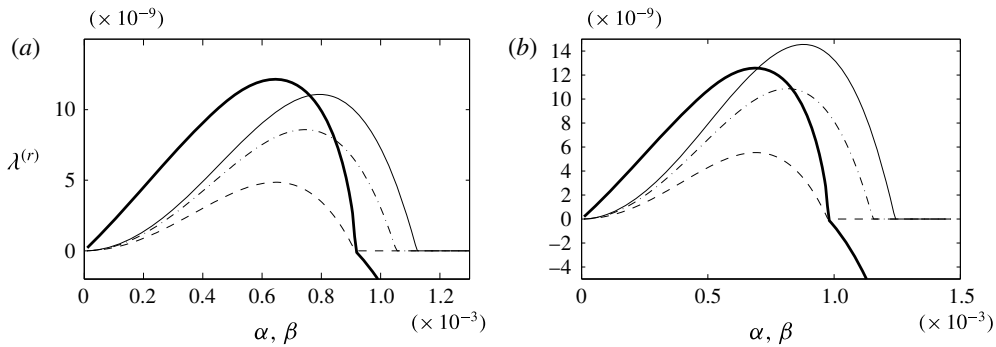


FIGURE 5. The growth rate plotted against the α -axis (thin lines) and β -axis (thick line). Plots against the α -axis: numerical computation (solid thin line), analytical computation (dashed thin line), numerical computation without convective terms (dash-dotted thin line). (a) Case A_K and $c = 5$ cm century $^{-1}$. (b) Case B_K and $c = 5$ cm century $^{-1}$.

that along the α -axis, when this latter is computed both numerically (thin line) and analytically (dashed line). On the contrary, in the ripple regime (case B_K , panel *b*), the thin solid line is higher than the thick one, but the dashed line still remains lower. Therefore, the analytical prediction of the curve $\lambda^{(r)}(\alpha)$ always underestimates the true behaviour and mirrors the behaviour on the β -axis, i.e. the outer contour line is nearly circular. The failure of the analytical model on the α -axis is a consequence of the two approximations contained in the Stokes problem, which both contribute to reducing the value of $\lambda^{(r)}$. The two effects can be separated by solving the problem while neglecting the convective terms but not the right-hand side of (3.6). The result of this latter choice is reported by the dot-dashed line in figure 5, which still remains remarkably different from the dashed line where both approximations have been made.

The above picture is completed by reporting the results for the ice case (figure 6). Figure 6(a) shows the numerical result concerning point A_I of figure 3(b) ($\gamma = 10^3$), where one can observe a large boundary layer centred on the β -axis (the width of which is again of order $\sim \gamma^{-1}$) and the absence of secondary peaks. Owing to the circularity of the outer contour line, once again the estimation given by the analytical formula (3.17) corresponding to $\beta_c \sim 0.005$ provides a good approximation for the critical longitudinal wavenumber, α_c . Figure 6(b) (point B_I , $\gamma = 10^4$) refers to a condition that is close to the fluting–ripple transition. In this case the circularity of the outer contour line is completely lost, as is evident by the distorted scales of the picture, but maxima are still on the β -axis and the γ^{-1} scaling of the internal boundary layer is still valid. Incidentally, we note that, if the behaviour along the α -axis is plotted (not shown), then a very weak relative maximum appears, but it is several orders of magnitude smaller than the dominant one on the β -axis. In figure 6(c) (point C_I , $\gamma = 2 \times 10^4$), the scenario is completely different, since it occurs in the ripple regime. The higher contour lines in fact appear centred on the α -axis at $\alpha \sim 0.03$, corresponding to a dimensional wavelength of nearly 5 cm. We observe that the plot reported in figure 6(c) extends to larger values of α and β than the previous cases, which means that the emerging patterns involve shorter wavelengths. In this case, the theoretical critical wavelength (3.17) does not predict correctly the border of the instability on the α -axis.

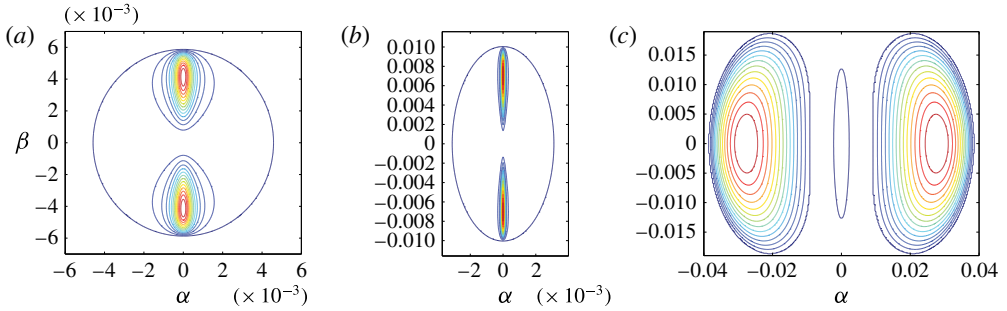


FIGURE 6. (Colour online) Contour plot from blue to red of $\lambda^{(r)}$ for the cases A_I (a), B_I (b) and C_I (c). The maximum value is also reported: (a) 1.1×10^{-6} ; (b) 3.2×10^{-6} ; (c) 3.5×10^{-4} .

It is worth noting that the maximum growth rate for the I case is numerically higher than for the K case; this is quite reasonable, since the time scales of the wall evolution are different in the two cases, as accounted for by the parameter γ , which has the same order of magnitude as λ^{-1} (see (3.8)).

At this point, we sum up the main results of the above analysis. (i) At the Reynolds numbers under investigation, the mathematical problem formulated in § 3.1 predicts pattern formation at only inverted conditions ($\vartheta > 0$). (ii) Provided the latter condition is satisfied, the results depend on the slope angle ϑ , as testified by the shape of the curve $Re_t(\vartheta)$. (iii) At $Re < Re_t$, the selected patterns are longitudinally oriented, i.e. flutes. (iv) Since the Stokes approximation is exact on the β -axis, the developed theoretical formulas can describe the fluting regime correctly. On the contrary, in the ripple regime ($Re > Re_t$) the numerical solution developed in § 3.2 is necessary. (v) These remarks are general and valid for both karst and ice problems, the only difference being quantitative and concerning the value of Re_t for the fluting–ripple transition and the width of the internal boundary region located around the β -axis. (vi) There is no bulb-like pattern formation corresponding to maxima out of the α -axis or β -axis.

The fundamental result is that the present model turns out to be a suitable tool for explaining fluting formation, provided $Re < Re_t$. The selected transverse wavenumbers are of order 10^{-3} , which corresponds to spanwise wavelengths of centimetres, whereas the dimensional time scale of the instability is $\tilde{\tau} \sim \tilde{D}_0 / \tilde{U}_0 \lambda_+^{(r)}(\beta_m)$, which yields $\tilde{\tau}_K = 14$ days and $\tilde{\tau}_I = 27$ min (for points A_K and B_I , respectively). The typical (spatial and temporal) scales of pattern inception are therefore captured for both problems (see also Martin-Perez, Martin-Garcia & Alonso-Zarza 2012; Chen 2014). Additionally, non-negligible (albeit non-dominant) values of $\lambda^{(r)}$ at $\alpha \neq 0$ are a clue to the longitudinal component of the instability, and the well-known presence of draperies in the K case and their absence in the I case support these results. We infer that this feature is dependent on the value of parameter γ .

The dots in figure 7(a) show the selected transverse wavelength \tilde{L}_y , as numerically computed, versus wall slope. Note that, because of the Re dependence of \tilde{D} , the dimensional outcome of \tilde{L}_y is unaffected by Reynolds number (which varies over two orders of magnitude in the figure). This feature is shared with speleothem dynamics (Camporeale & Ridolfi 2012a) and could justify the pattern regularity and the lack of noise in the shapes observed, since any seasonal or inter-annual variation in the flow

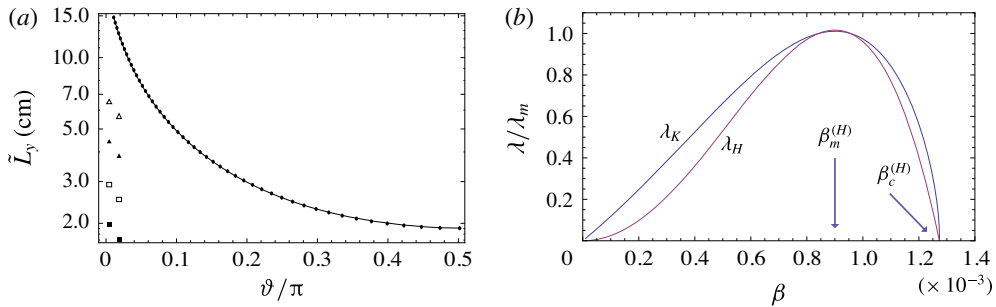


FIGURE 7. (Colour online) (a) Dimensional transverse wavelength versus ϑ ($Re = [10^{-3}-10^{-1}]$, $c = [1-5]$ cm century $^{-1}$): MOS model (dots, either ice and karst case); fixed-bed model ($\tilde{L}_y^{(H)}$, continuous line); and non-parallel theory ($\tilde{L}_y^{(G)}$), for $Re = 0.03$ (full symbols) or 0.3 (open symbols) with $\mathcal{R} = 2$ m (squares) or 10 m (triangles), and $T = 273$ K (left row) or $T = 288$ K (right row). (b) Normalized growth factor versus β for the case A_K , where arrows indicate the value given by (3.26).

does not force significant changes on the selected length scale. However, we will see in §4 that a weak dependence on the Reynolds number arises when wall curvature is accounted for. Furthermore, the results are also γ -independent (both cases are in fact reported in figure 7) which is a first symptom of HLM, a feature that will be definitively proved in the next section.

Although the focus of the present work is on the fluting regime, some remarks on ripple formation are due. In the karst problem, the emergence of ripples, also called crenulations, confirms the findings by Camporeale & Ridolfi (2012a), where a novel model successfully predicted the formation of ripple-like undulations on the surface of stalactites, by considering hydrodynamics, calcium and carbon dioxide geochemistry in detail. Despite the fact that the present model does not consider at all the dynamics of solutes (apart from the phenomenological evolution equation (2.11)), its ability to predict crenulations is confirmation of the recent remarks by Vesipa, Camporeale & Ridolfi (2015), where a thorough sensitivity analysis has shown that a correct modelling of free surface dynamics is sufficient to provide successful predictions.

As far as the ice problem is concerned, the ripple regime can be assimilated to the so-called icicles. Past theoretical works have explained the formation of icicles by pure water falling films (e.g. Ueno *et al.* 2010), but the recent experimental findings by Chen & Morris (2013) have questioned whether pure water is able to trigger icicle formation. The experiments in fact required the presence of dissolved salts in order to see appreciable instabilities. Likewise, the reliability of the ripple regime that is herein theoretically predicted could be questioned too. Yet, it is worthwhile to compute the value of the Reynolds number corresponding to the experiments conducted by Chen & Morris (2013). They reported a water flow rate $q = 3$ g min $^{-1}$ or less. Assuming a centimetre stalactite diameter, ϕ , this is equivalent to $Re = q/2\pi\phi\nu = O(10^{-2})$. When reported in figure 3(b), this value falls in the fluting regime, which could explain why the experiments did not produce icicles. If confirmed by further experiments made at higher values of Reynolds number, this argument might resolve the debate opened by the experimental results by Chen & Morris (2013). Nevertheless, it remains to be explained why dissolved salt is a destabilizing factor.

3.5. The fixed-bed model and the HLM conjecture

We now demonstrate that the geometrical structure of the fluting instability is completely driven by film hydrodynamics of inverted flows. To this end, we neglect the contribution of the wall evolution equation (2.3) and consider standard fixed-bed conditions (i.e. no slip and impermeability), in place of (3.4). This is formally equivalent to setting $\gamma^{-1} \rightarrow 0$. Since fluting formation is addressed here, henceforth we will focus only on spanwise wavelength selection ($\alpha = 0$). The model (3.3)–(3.8) therefore reduces to

$$\left(\frac{d^4}{d\zeta^4} - 2\beta^2 \frac{d^2}{d\zeta^2} + \beta^4 \right) \hat{\phi} = 0 \quad (0 \leq \zeta \leq 1), \tag{3.18}$$

$$\hat{\phi} = \frac{d\hat{\phi}}{d\zeta} = 0 \quad (\zeta = 0), \tag{3.19}$$

$$\left(\frac{d^2}{d\zeta^2} + \beta^2 \right) \hat{\phi} = 0 \quad (\zeta = 1), \tag{3.20}$$

$$\frac{d}{d\zeta} \left(\frac{d^2}{d\zeta^2} - 3\beta^2 \right) \hat{\phi} - \Omega = 0 \quad (\zeta = 1), \tag{3.21}$$

$$i\lambda - \beta\hat{\phi} = 0 \quad (\zeta = 1). \tag{3.22}$$

The above mathematical problem refers to a purely hydrodynamic fixed-bed modelling, which has fully lost the morphological mode of the MOS and Stokes models, as well as the ability to catch the temporal dynamics of pattern formation. Notwithstanding this, our aim is to show that the geometrical features of the selected patterns are preserved through the action of the hydrodynamic mode, which is the essence of the HLM.

The solution of (3.18)–(3.21) is

$$\hat{\phi} = \Omega \frac{2\beta^2\zeta(e^{2\beta} - e^{2\beta\zeta}) + \beta e^{2\beta}[(\zeta - 1)e^{2\beta\zeta} + (\zeta + 1)(e^{2\beta\zeta} + 1)](e^{2\beta} + 1)(e^{2\beta\zeta} - 1) + \beta\zeta - 1}{4\beta^3 e^{\beta(\zeta+1)}(2\beta^2 + \cosh(2\beta) + 1)}. \tag{3.23}$$

The use of (3.22) yields the hydrodynamic growth factor (hereafter denoted by H)

$$\lambda_r^{(H)} = \frac{(\beta - \sinh \beta \cosh \beta)[2^{1/3} Ka Re^{-2/3} \beta^2 \sec \vartheta^{1/3} - 2 \tan \vartheta]}{\beta[1 + 2\beta^2 + \cosh(2\beta)]}. \tag{3.24}$$

In figure 7(b), the result provided by (3.24) is compared to the growth rates obtained by the MOS problem for the K case, under the conditions of case A_K . Since the focus here is on the dependence of the growth factor on β , the ordinate has been rescaled by the maximum value of each curve, λ_m . It is remarkable that, despite some small differences in the shape, the values of the largest unstable wavenumber, β_c , and the wavenumber that maximizes the instability, β_m , coincide among the three curves. The same behaviour can be obtained if comparisons are made with the ice case. It follows that the hydrodynamic theory evaluates the same wavelengths selected as the morphodynamic theories, regardless of the value of γ .

Accordingly, we take advantage of (3.24) to analytically derive formulas for: (i) the critical wavenumber β_c , by setting $\lambda_r^{(H)}(\beta_c) = 0$, and (ii) the most unstable wavenumber

β_m , by setting $d\lambda_r^{(H)}/d\beta = 0$. After Taylor-expanding in β (owing to the reasonable assumption $\beta \ll 1$), one obtains

$$\frac{\partial \lambda_r^{(H)}}{\partial \beta} = \frac{4}{3}\beta \left[-\beta^2 \left(\frac{2^{1/3}Ka \sec \vartheta^{1/3}}{Re^{2/3}} + \frac{18}{5} \tan \vartheta \right) + \tan \vartheta \right] + O(\beta^5). \tag{3.25}$$

From (3.24) and (3.25), we arrive at

$$\beta_c^{(H)} = \frac{(2Re \sec \vartheta)^{1/3}}{\sqrt{Ka}} \sqrt{\sin \vartheta}, \quad \beta_m^{(H)} \sim \left(2^{4/3}Ka \sin \vartheta (Re \sec \vartheta)^{2/3} + \frac{18}{5} \right)^{-1/2}. \tag{3.26a,b}$$

Recalling that $Re \ll 1$, (3.26a) gives

$$\beta_m = \frac{(Re \sec \vartheta)^{1/3}}{2^{1/6}\sqrt{Ka} \csc \vartheta} \implies \tilde{L}_y^{(H)} = 2\pi l_c \sqrt{2 \csc \vartheta}. \tag{3.27}$$

For the particular case $\vartheta = \pi/2$, this latter result corresponds to the Rayleigh–Taylor instability, namely $\tilde{L}_y = 2\pi l_c \sqrt{2} \sim 8.8l_c$ (Charru 2001). The behaviour of $\tilde{L}_y^{(H)}$ is reported in figure 7(a) with a continuous line. Remarkably, despite its simplicity, equation (3.27) completely agrees with the MOS theory (dots). In order to better appreciate this comparison, the relative difference between $\tilde{L}_y^{(H)}$ and the wavelength selected by the MOS theory has been computed for $Re = [10^{-3}–10^{-1}]$ and $c = [1–5] \text{ cm century}^{-1}$, obtaining a relative error always smaller than 10^{-4} . This latter test furnishes the ultimate proof of the HLM conjecture.

4. Non-parallel stability theory

According to the local stability analysis developed so far, \tilde{L}_y diverges for vertical flows (i.e. when ϑ approaches zero), so no wavelength is selected close to the critical condition and the formulas reported in the previous section are only valid for $\vartheta > 0$. Another criticism is that the flow-induced morphological channelization is triggered at the upper boundary of the unstable zone, namely where the azimuthal coordinate θ is zero. These shortcomings can be definitively remedied through a refined non-parallel stability analysis, which also encloses the radius of curvature $\tilde{\mathcal{R}}$ of the wall and non-parallelism of the flow field, in a neighbourhood of the vertical tangent point (figure 2). In order to simplify the analysis, we will axiomatically assume that, in the limit of small curvature, the HLM is also valid for the non-parallel case. Therefore, the analysis will be focused on the fixed-bed case, in the fluting regime, with no distinction between the karst and ice cases.

If all quantities are scaled with film depth and surface velocity at $\theta = 0$, a new parameter emerges, namely the dimensionless curvature $\mu = (\tilde{D}/\tilde{\mathcal{R}})_{\theta=0}$. Since $\mu \ll 1$, we are allowed to simplify several relationships that will be derived in the following. It is convenient to adopt cylindrical coordinates $\{\theta, r, y\}$, as depicted in figure 2. Accordingly, the velocity vector becomes $\mathbf{u} = \{u_\theta, u_r, u_y\}$ and the mathematical problem is recast in the form

$$\frac{1}{r} \frac{\partial p}{\partial \theta} - \frac{1}{Re} \left(\nabla^2 u_\theta + \frac{2}{r^2} \frac{\partial u_r}{\partial \theta} - \frac{u_\theta}{r^2} \right) - 2 \frac{\sin \theta}{Re} = 0, \tag{4.1}$$

$$\frac{\partial p}{\partial r} - \frac{1}{Re} \left(\nabla^2 u_r - \frac{2}{r^2} \frac{\partial u_\theta}{\partial \theta} - \frac{u_r}{r^2} \right) - 2 \frac{\cos \theta}{Re} = 0, \tag{4.2}$$

$$\frac{\partial p}{\partial y} - \frac{1}{Re} \left(\frac{\partial^2 u_y}{\partial \theta^2} + \frac{\partial^2 u_y}{\partial y^2} + \frac{\partial^2 u_y}{\partial r^2} \right) = 0, \tag{4.3}$$

$$\frac{\partial}{\partial r}(ru_r) + r \frac{\partial u_y}{\partial y} + \frac{\partial u_\theta}{\partial \theta} = 0, \tag{4.4}$$

where $\nabla^2 \equiv r^{-2} \partial_{\theta\theta} + r^{-1} \partial_r(r \partial_r) + \partial_{yy}$ (Batchelor 1967, p. 602). The boundary conditions read

$$\mathbf{u} = 0 \quad (r = \mathcal{R}), \tag{4.5}$$

$$D_r + \frac{u_\theta}{r} D_\theta + u_y D_y - u_r = 0 \quad (r = \mathcal{R} + D), \tag{4.6}$$

$$\mathbf{n} \cdot \mathbf{D} \cdot [\mathbf{t}_x \mathbf{t}_y] = 0 \quad (r = \mathcal{R} + D), \tag{4.7}$$

$$p - 2 Re^{-1} (\mathbf{n} \cdot \mathbf{D} \cdot \mathbf{n}) + 2^{1/3} Ka Re^{-5/3} \mathcal{K}_S = 0 \quad (r = \mathcal{R} + D), \tag{4.8}$$

where \mathbf{n} and \mathbf{t}_x are respectively the vectors $\{r^{-1} D_\theta, -1, D_y\}$ and $\{1, r^{-1} D_\theta, 0\}$, normalized by their absolute values, while $\mathbf{t}_y = \mathbf{t}_x \times \mathbf{n}$, the subscripts of D refer to partial derivatives, and the rate-of-strain tensor reads

$$\mathbf{D} = \begin{pmatrix} \frac{1}{r} \frac{\partial u_\theta}{\partial \theta} + \frac{u_r}{r} & \frac{1}{2} \left(-\frac{\partial u_\theta}{\partial y} - \frac{1}{r} \frac{\partial u_y}{\partial \theta} \right) & \frac{1}{2} \left(\frac{u_\theta}{r} - \frac{\partial u_\theta}{\partial r} - \frac{1}{r} \frac{\partial u_r}{\partial \theta} \right) \\ -\frac{\partial u_\theta}{\partial y} - \frac{1}{r} \frac{\partial u_y}{\partial \theta} & \frac{\partial u_y}{\partial y} & \frac{1}{2} \left(-\frac{\partial u_y}{\partial z} - \frac{\partial u_r}{\partial y} \right) \\ \frac{1}{2} \left(\frac{u_\theta}{r} - \frac{\partial u_\theta}{\partial z} - \frac{1}{r} \frac{\partial u_r}{\partial \theta} \right) & \frac{1}{2} \left(-\frac{\partial u_y}{\partial z} - \frac{\partial u_r}{\partial y} \right) & \frac{\partial u_r}{\partial r} \end{pmatrix}. \tag{4.9}$$

Prandtl’s mapping is posed in the form $r = \zeta d + \mu^{-1}$, thus the solution ansatz of a generic quantity f (e.g. depth, velocity and pressure) is recast in a global-mode fashion,

$$f(\theta, \zeta, y, t; \mu) = f_0(\theta, \zeta; \mu) + \epsilon \hat{f}(\theta, \zeta; \mu) \exp[\lambda^{(\mathcal{G})} t + i\beta y], \tag{4.10}$$

where the explicit dependence on θ accounts for non-parallel effects, whereas the basic state $O(\epsilon^0)$ can be further expanded in powers of μ up to the first order, namely $f_0 = f_{00}(\theta, \zeta) + \mu f_{01}(\theta, \zeta)$. In the present non-parallel theory, (4.10) is a generalization of (3.1). Note that in a standard global stability analysis the azimuthal coordinate θ also appears in the exponential, through a multiple scaling approach, and the problem is then tackled through the WKBJ technique (Huerre & Rossi 1998). Since we are only interested to the longitudinally parallel perturbations (flutes), this trick can be avoided. Moreover, a detailed order-of-magnitude analysis of continuity equation (4.4) suggests that, at the basic state, the radial component of velocity is at most of order μ , and its correct ansatz at the order $O(\epsilon^0)$ is therefore $u_{r,0} = \mu u_{r01}(\theta, \zeta) + \mu^2 u_{r02}(\theta, \zeta)$.

4.1. Problem $O(\epsilon^0)$

The equations at leading order pose $\epsilon = \mu = u_{y00} = 0$ and therefore read

$$\frac{\partial^2 u_{\theta 00}}{\partial \zeta^2} + 2(1 + D_{00})^2 \cos \theta = 0, \tag{4.11}$$

$$Re \frac{\partial p_{00}}{\partial \zeta} - 2(1 + D_{00}) \sin \theta = 0, \tag{4.12}$$

$$(1 + D_{00}) \frac{\partial u_{\theta 00}}{\partial \theta} - \zeta D'_{00} \frac{\partial u_{\theta 00}}{\partial \zeta} + \frac{\partial u_{r01}}{\partial \zeta} = 0, \tag{4.13}$$

$$u_{\theta 00} = u_{r01} = 0 \quad (\zeta = 0), \tag{4.14}$$

$$D'_{00} u_{\theta 00} - u_{r01} = 0 \quad (\zeta = 1), \tag{4.15}$$

$$\frac{\partial u_{\theta 00}}{\partial \zeta} = p_{00} = 0 \quad (\zeta = 1), \tag{4.16}$$

where the prime refers to the θ derivative. The above set of equations is readily solved, yielding

$$D_{00} = (\sec \theta)^{1/3}, \quad u_{\theta 00} = \frac{u_0}{D_{00}}, \quad u_{r01} = \frac{u_0 \zeta}{3} \tan \theta, \quad p_{00} = -\frac{u'_0 D_{00}}{Re} \sin \theta, \tag{4.17a-d}$$

where $u_0 = 2\zeta - \zeta^2$ is the Nusselt parabolic profile, which was already derived in the parallel problem.

After substituting (4.17) and collecting the terms of order $O(\epsilon^0 \mu^1)$, one obtains the problem

$$\frac{\partial^2 u_{\theta 01}}{\partial \zeta^2} + 4(\cos \theta)^{2/3} D_{01} + \frac{2}{3}[5 - 6\zeta + (\sec \theta)^2] = 0, \tag{4.18}$$

$$Re \frac{\partial p_{01}}{\partial \zeta} - 2D_{01} \sin \theta + 2(3\zeta - 2) \frac{\sin \theta}{3 \cos \theta^{2/3}} = 0, \tag{4.19}$$

$$\frac{\zeta}{3} [D_{01}(9\zeta - 14)\Upsilon_2 + 6D'_{01}(\cos \theta)^{1/3} + \Upsilon_1] + \frac{\partial u_{r02}}{\partial \zeta} = 0, \tag{4.20}$$

$$u_{\theta 01} = u_{r02} = 0 \quad (\zeta = 0), \tag{4.21}$$

$$D'_{01} - \frac{2 \tan \theta}{7} D_{01} + \Upsilon_3 = 0 \quad (\zeta = 1), \tag{4.22}$$

$$\frac{\partial u_{\theta 01}}{\partial \zeta} - (\cos \theta)^{1/3} = 1, \quad Re p_{01} - \frac{2}{3} \Upsilon_2 - Ka \left(\frac{4}{Re} \right)^{2/3} = 0 \quad (\zeta = 1), \tag{4.23a,b}$$

where

$$\Upsilon_1 = \frac{[2(5 - 2\zeta) \sec \theta^2 - (18\zeta^2 - 28\zeta + 7)] \sin \theta}{3(\cos \theta)^{4/3}}, \tag{4.24a}$$

$$\Upsilon_2 = \frac{\sin \theta}{(\cos \theta)^{2/3}}, \quad \Upsilon_3 = \frac{\cos(3\theta) + 9 \sin \theta}{36(\cos \theta)^{11/3}}. \tag{4.24b,c}$$

The complete solution of (4.18)–(4.23) is

$$D_{01} = \frac{7[33(\cos \theta)^{8/21} - 8 \sec^2 \theta - 25]}{600(\cos \theta)^{2/3}}, \tag{4.25}$$

$$u_{\theta 01} = -\frac{1}{3} \zeta [18D_{01}(\zeta - 2)(\cos \theta)^{2/3} + (\zeta - 2)(\sec \theta)^2 - \zeta(2\zeta - 5) - 7], \tag{4.26}$$

$$p_{01} = \frac{10D_{01}}{Re} (\zeta - 1) \sin \theta + \frac{12Ka(\cos \theta)^{2/3} + 2^{2/3}((4 - 3\zeta)\zeta + 1) Re^{2/3} \sin \theta}{3 Re(Re \sin 2\theta \csc \theta)^{2/3}}, \tag{4.27}$$

$$u_{r02} = \frac{\zeta^2[72(\zeta - 3) \cos^{11/3}(\theta)D_{01}']}{108(\cos \theta)^{10/3}} + \frac{\zeta^2 \sin \theta[(36(7 - 3\zeta)D_{01} \cos^{8/3} \theta + (\zeta(27\zeta - 56) + 21) \cos 2\theta + \zeta(27\zeta - 40) - 39)]}{108(\cos \theta)^{10/3}}. \tag{4.28}$$

The sum $D_{00} + \mu D_{01}$ provides an approximate solution of the depth, up to order μ , for the non-parallel base state problem and, to the author’s knowledge, is a novel result for the present geometry. It should be noted that the first term corresponds to the uniform Nusselt’s solution computed at a varying slope $\theta(s) \neq \vartheta$. The flow is actually well approximated by this solution (also called normal solution) when μ is small, namely when θ changes slowly in the streamwise direction due to the small curvature of the wall. The normal solution has a minimum $D_{00} = 1$ at the vertical tangent point, $\theta = 0$, and it results from a balance between the streamwise component of the gravity force, the pressure gradient and the basal shear stress. At the order μ , normal viscous stresses acting on the vertical planes play a role in smoothing the free surface curvature, and they slightly reduce its deviation from the value obtained at the vertical tangent point. This means that D_{01} always gives a negative contribution. By using the relations in (4.17) and (4.25) it is straightforward to compute the relative deviation between the normal D_{00} solution and its correction μD_{01} , which is at most $\sim 0.15\mu$ for $|\theta| < \pi/4$. Since in the present analysis μ will be considered of order 10^{-3} or less, the correction to the normal solution is not relevant, despite its theoretical value and applicability to other problems. One could therefore neglect the effects of this term in the following development of the perturbed problem. However, we prefer to keep it in the following derivation, in order to pose the analysis in a more general way.

4.2. Problem $O(\epsilon)$: the global eigenvalue

The problem at order $O(\epsilon)$ is much more involved, but it can be addressed quite easily by recognizing that the term related to the mass forces is wholly absorbed at the leading order and the Stokes flow problem, written at order ϵ , reduces to the search for a solution of the equation $\nabla^2 \hat{\mathbf{u}} = Re^{-1} \nabla \hat{p}$ posed in a cylindrical reference frame. This allows us to use the Papkovitch–Neuber solutions (Tran-Cong & Blake 1982) to the perturbed quantities,

$$\hat{\mathbf{u}} = \nabla(\mathbf{r} \cdot \Psi + \Psi_0) - 2\Psi, \quad \hat{p} = 2Re^{-1} \nabla \cdot \Psi, \tag{4.29a,b}$$

where $\mathbf{r} = r\{\cos \theta, \sin \theta\}$, and $\Psi = \{\Psi_\theta, \Psi_r\}$ and Ψ_0 are harmonic potentials (Ψ_r is set to zero because of the transverse invariance), which satisfy the following equations:

$$\frac{\partial^2 \Psi_\theta}{\partial \theta^2} - \Psi_\theta + r \left[\frac{\partial}{\partial r} \left(r \frac{\partial \Psi_\theta}{\partial r} \right) + r \frac{\partial^2 \Psi_\theta}{\partial y^2} \right] + 2 \frac{\partial \Psi_r}{\partial \theta} = 0, \tag{4.30}$$

$$\frac{\partial^2 \Psi_r}{\partial \theta^2} - \Psi_r + r \left[\frac{\partial}{\partial r} \left(r \frac{\partial \Psi_r}{\partial r} \right) + r \frac{\partial^2 \Psi_r}{\partial y^2} \right] - 2 \frac{\partial \Psi_\theta}{\partial \theta} = 0, \tag{4.31}$$

$$\frac{\partial^2 \Psi_0}{\partial \theta^2} + r \left[\frac{\partial}{\partial r} \left(r \frac{\partial \Psi_0}{\partial r} \right) + r \frac{\partial^2 \Psi_0}{\partial y^2} \right] = 0. \tag{4.32}$$

The above equations are solved by invoking once again the global-mode ansatz

$$\Psi_j = \epsilon \hat{\Psi}_j(\theta, r, y) \exp[\lambda^{(G)}t + i\beta y] \quad (j = 0, \theta, r). \tag{4.33}$$

After substituting (4.33) in (4.30)–(4.32), using the Prandtl mapping ($r \rightarrow \zeta$) and expanding up to the first order in ϵ and μ , the three harmonic equations for the perturbation mode of potentials reduce to

$$\frac{\partial^2 \hat{\Psi}_j}{\partial \zeta^2} + \mu D_{00} \frac{\partial \hat{\Psi}_j}{\partial \zeta} - \beta^2 D_{00}^2 \hat{\Psi}_j = 0 \quad (j = \theta, r, 0). \tag{4.34}$$

By recalling that $D_{00} = (\sec \theta)^{1/3}$ and $\theta = \mu s$, the approximate solutions of (4.34) are

$$\hat{\Psi}_j(s, \zeta) = C_j^\pm(s) \exp[\pm(\beta - \mu/2)\zeta + O(\mu^2)] \quad (j = 0, \theta, r). \tag{4.35}$$

The coefficients C_j^\pm are obtained by imposing no slip and impermeability at $\zeta = 0$ and the dynamic conditions at $\zeta = 1$ (i.e. the $O(\epsilon)$ order version of (4.5) and (4.7), written in the new coordinate system), which read, respectively,

at $\zeta = 0$

$$\begin{bmatrix} \mu & -\frac{1}{2} \frac{\partial}{\partial s} & -\mu \frac{\partial}{\partial \zeta} \\ 0 & -\mu + \frac{\partial}{\partial \zeta} & 0 \\ 0 & 1 & \mu \end{bmatrix} \begin{pmatrix} \hat{\Psi}_\theta \\ \hat{\Psi}_r \\ \hat{\Psi}_0 \end{pmatrix} = 0, \tag{4.36}$$

at $\zeta = 1$

$$\begin{bmatrix} \mu - \frac{\partial}{\partial \zeta} & \left[\mu - 1 + \left(\frac{1}{\mu} - 2\mu \right) \frac{\partial}{\partial \zeta} \right] \frac{\partial}{\partial s} & \left[\left(1 - \frac{\mu}{2} \right) \frac{\partial}{\partial s} - \mu \right] \frac{\partial}{\partial \zeta} \\ 0 & (5\mu^2 - \mu - 1) \frac{\partial}{\partial \zeta} + \frac{\mu s^2}{6} \frac{\partial}{\partial \zeta} & \mu \frac{\partial}{\partial \zeta} \\ \frac{\partial}{\partial s} & \mu + \left(1 + \mu s \frac{\partial}{\partial s} - \frac{1 + \mu}{\mu} \frac{\partial}{\partial \zeta} \right) \frac{\partial}{\partial \zeta} & -\frac{\partial^2}{\partial \zeta^2} \end{bmatrix} \begin{pmatrix} \hat{\Psi}_\theta \\ \hat{\Psi}_r \\ \hat{\Psi}_0 \end{pmatrix} = \begin{pmatrix} \mu \\ 0 \\ \frac{Ka\beta^2}{(2Re)^{2/3}} \end{pmatrix} \hat{D}. \tag{4.37}$$

After substituting (4.35) in (4.36) and (4.37) and solving, it follows that $C_j^\pm = c_j^\pm \hat{D}(s)$, with $j = \{\theta, r, 0\}$. If a truncated series expansion in μ and β is performed (recall in fact that $\beta \ll 1$), the coefficients c_j^\pm read

$$c_\theta^\pm = \pm \frac{\mu}{24\beta} \left[\beta^2 \left(\frac{\sqrt[3]{2} Kas}{Re^{2/3}} - 3 \right) + 6 \right], \quad c_r^\pm = \mp \frac{\beta Ka [\beta(2 \mp 8\mu) + \mu + 2]}{2^{5/3} Re^{2/3}}, \tag{4.38a,b}$$

$$c_0^\pm = \pm \frac{\beta Ka \{ \beta [\pm 8 - \mu(109\mu + 32)] \pm 3(4 - 29\mu)\mu + 8 \}}{16 \cdot 2^{2/3} \mu Re^{2/3}}. \tag{4.39}$$

It is worth recalling that $\hat{D}(s)$ is the global mode of depth perturbation and it plays the role of the unknown eigenfunction of the problem. After plugging all this in the

kinematic condition (4.6) and applying the aforementioned transformations, we finally get a first-order differential eigenvalue problem relating $\hat{D}(s)$ and $\lambda^{(G)}$ in the form

$$\left[\frac{\partial}{\partial s} + \frac{\mathcal{F}(s) + \lambda^{(G)}}{1 + \varrho s} \right] \hat{D} = 0, \tag{4.40}$$

where the coefficient ϱ and the function $\mathcal{F}(s)$ depend in a complicated manner upon μ and β . Since (4.40) is formally solvable by a separation of variables, its solution is proportional to the boundary condition $\hat{D}(0)$, which can therefore be absorbed by the prefactor ϵ , by putting $\hat{D}(0) = 1$. It is also evident that the eigenvalue must satisfy the relation $\lambda^{(G)} = -\mathcal{F}(0) - \hat{D}'(0)$, whence a continuous spectrum of eigenvalues parametrized by the quantity $\hat{D}'(0)$ emerges. A reasonable choice is to put $\hat{D}'(0) = 0$ since, in this manner, it can be shown that the solution (4.40) is the most regular one (i.e. the average value of $\hat{D}(s)$ is minimized). We therefore arrive at our main goal, namely the solution of the global eigenvalue

$$\lambda^{(G)} = -\mathcal{F}(0) = \frac{\beta(63\mu + 8) \cosh \beta - [\beta^2(77\mu + 8) + 4(\mu + 2)] \sinh \beta}{8(2Re)^{2/3}} \beta K a e^{-\mu/2}. \tag{4.41}$$

Inspection of the dependence of (4.41) on β , in the range $\beta \ll 1$, shows that there is a maximum (the selected wavenumber) at $\beta_m^{(G)} \sim \sqrt{177\mu}/4\sqrt{2}$ and a zero value (the cutoff) at $\beta_c^{(G)} = \sqrt{2}\beta_m^{(G)}$. This amazing result translates into a dimensional selected wavelength that reads

$$\tilde{L}_y^{(G)} \sim 3\nu^{1/3} \left(\frac{Re}{g} \right)^{1/6} \tilde{\mathcal{R}}^{1/2}. \tag{4.42}$$

The latter formula provides a finite wavelength selection at finite values of dome radius of curvature. A novel weak Re dependence has appeared in (4.42), through a one-sixth power law. The effect of the capillary length, which is crucial in planar conditions, is therefore replaced by $\tilde{\mathcal{R}}$ when curvature is considered. Physically speaking, the effect of surface tension is overwhelmed by streamwise momentum diffusion, because of non-parallel effects. The symbols in figure 7(a) provide some computations of (4.42); for example, $\tilde{L}_y^{(G)} = 3$ cm for $\tilde{\mathcal{R}} = 2$ m and $Re = 0.3$.

A possible scenario is that the patterns are triggered at wavelength $\tilde{L}_y^{(G)}$ around $s=0$, where $\theta = 0$ and the curvature is maximum, then fluting spacing gradually converges downstream to the value provided by $\tilde{L}_y^{(H)}$, where the wall becomes almost planar. The non-parallel theory presented herein has therefore resolved the inconsistency observed with the parallel theory: finite wavelengths can be selected at $\theta = 0$.

5. Discussion

Let us summarize the key steps presented. First, a simple evolution law for the wall dynamics – namely, (2.3) in dimensional form or (2.11) in dimensionless form – has been obtained for both karst and ice systems; therefore these two geophysical problems can be dealt with in a unified mathematical framework, once the parameter γ is given. Second, at low Reynolds numbers, pattern formation occurs at inverted conditions only and the fluting–ripple transition is identified by the curve $Re_t(\theta)$. The correct evaluation of this transition has required a rigorous numerical solution of the Orr–Sommerfeld-like problem. Apparently, the fluting regime violates Squire’s

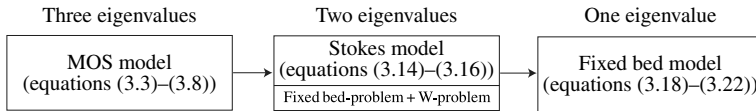


FIGURE 8. Hierarchy of models in the parallel stability theory.

theorem. Third, wavelength selection in the fluting regime can be investigated analytically through the lubrication theory. Fourth, the HLM conjecture has been proved to be correct in the fluting regime, since a fixed-bed model selects the same transverse wavelength of the complete model (which correctly reduces to the Rayleigh–Taylor instability when $\vartheta \rightarrow \pi/2$). Fifth, close to verticality, the non-parallel theory yields finite values of the selected wavelength, thus resolving a shortcoming of the parallel theory.

In the following we will briefly address two questions that arise from the above picture: (i) Which mechanisms underlie the HLM conjecture? (ii) How are the parallel and non-parallel theories related to each other?

The first question can be tackled by recalling the hierarchy of three models we have analysed in the parallel stability theory (see the scheme reported in figure 8): (i) the MOS model (3.3)–(3.8), solved numerically; (ii) a simplified version of the MOS model, based on the Stokes approximation, reported in § 3.3 and solved analytically; (iii) a further simplified model based on purely hydrodynamic equations (the fixed-bed model). All these models essentially require the solution of an eigenvalue problem. The complete model exhibits three temporal derivatives, which are related to the occurrence of three discrete eigenvalues, among which only one has a positive real part. Since we have neglected the temporal derivative in the dynamic condition (3.6), the Stokes model provides just two eigenvalues, which are related to the kinematics of the free surface and the wall evolution, namely (3.7) and (3.8), respectively. In the fixed-bed model, only one eigenvalue survives, which is related to the free surface kinematic equation. Owing to the HLM, the latter model catches the same transverse wavenumber as the complete one. It follows that the kinematic equation is essential in routing the fluting instability whereas the wall evolution is slaved to the free surface dynamics, without adding any other unstable behaviour. This means that the free surface triggers an unstable mode, while the wall triggers a stable mode.

A physical justification of the HLM is as follows. Let us focus on the Stokes model, which accounts for both the free surface kinematics and wall evolution (the role of the dynamic conditions can be safely neglected for a qualitative explanation) and consider the fluting condition only ($\alpha = 0$). The theory being linear, the solution can be thought of as the sum of two contributions: (i) a free surface-induced solution (coincident with the fixed-bed model), where the wall evolution is switched off and (ii) a wall-induced solution (referred to henceforth using the letter W), where the kinematic condition on the free surface reduces to $\hat{w}(1) = 0$, namely the free surface is as frozen. These two contributions are illustrated in figure 9 for a particular parametric case, whose the relation dispersion is reported in panel (d). In the fixed-bed problem (panel a), when the free surface is perturbed downwards, gravity induces fluid particles to converge towards the centre, resulting in a positive vertical velocity pointing to the maximum depth. This flow kinematically pushes the free surface further down, as modelled by the kinematic condition, and the instability is reinforced. Such a destabilizing mechanism is only possible at inverted (overhung) flows; it is smoothed out by

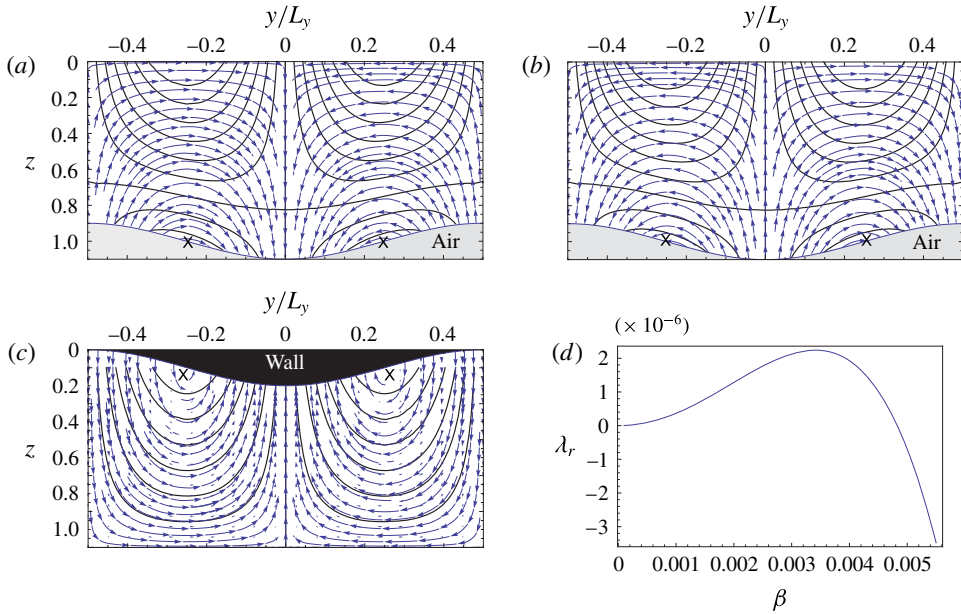


FIGURE 9. (Colour online) Streamlines (arrows) and vorticity (solid contours) reported from a frontal view for the karst case at $\vartheta = \pi/6$ and $Re = 0.01$ (axes not to scale). (a) Results from the fixed-bed model where the free surface is perturbed downwards with an arbitrary amplitude $\epsilon = 0.05$ at the most unstable wavenumber $\beta = 0.0034$. (b) Same as panel (a), but at stable conditions $\beta = 0.0068$. (c) Results from model W where the free surface is at rest and the wall is perturbed with an arbitrary amplitude $\epsilon = 0.05$ and wavenumber $\beta = 0.0034$. (d) Growth rate versus wavenumber as predicted by the fixed-bed model.

momentum diffusion and halted by surface tension. This latter in fact raises the fluid pressure when surface curvature increases (so-called Young–Laplace effect), so in the Fourier domain it is a $\sim \beta^2$ order process. Therefore gravity-driven flows are blocked when high wavenumbers are considered, as reported in figure 9(b).

The destabilization of the free surface is also evident if the longitudinal vorticity $\varphi(y, z) = w_{,y} - v_{,z}$ is considered (see solid contour lines in figure 9). Its Fourier mode in the rectangularized domain is given by $\hat{\varphi} = \beta^2 \hat{\phi}(\zeta) - \phi''(\zeta)$ and satisfies the vorticity equation $\hat{\varphi}'' - \beta^2 \hat{\varphi} = 0$. The boundary conditions for the fixed-bed problem read

$$\hat{\varphi}(0) = -\hat{\phi}''(0), \quad \hat{\varphi}(1) = \hat{\phi}(1), \tag{5.1a,b}$$

with

$$\hat{\phi}''(0) = -\frac{2\Omega \cosh \beta}{2\beta^2 + \cosh 2\beta + 1}, \quad \hat{\phi}(1) = \frac{\Omega(\beta - \sinh \beta \cosh \beta)}{\beta^3(2\beta^2 + \cosh 2\beta + 1)}, \tag{5.2a,b}$$

where (5.2a,b) follow from (3.23). The vorticity equation allows one to identify two counter-rotating vortices localized on the free surface at $y = \pm L_y/4$ that act dynamically to reinforce free surface instability (see crosses in figure 9a). It is straightforward to see from the solution to (5.1b) and (5.2b) that the sign of the vorticity at $\zeta = 1$ depends just on the term Ω , so the two vortices switch when

$\Omega(\beta) = 0$, namely when the capillarity term in Ω balances the gravity term. This latter condition is in fact another way to obtain the formula (3.26a), which governs the switching from unstable to stable wavenumbers (respectively, positive versus negative vorticity at the free surface).

On the contrary, when the free surface is frozen and the W problem is analysed, two vortices are confined to the wall at $y = \pm L_y/4$, thus inducing a circulating flow from the deeper zones towards the centre (see crosses in figure 9c). Since the vertical velocity is in this case forced to be zero on the free surface, the flow is collected towards the wall. Note that the wall-normal velocity is slightly different from zero because of the kinematic condition at $\zeta = 0$ via (3.4a). At the free surface, the converging flow is related to a lateral pressure gradient with a depletion of p at $y = 0$. Through the Young–Laplace effect, this induces a negative curvature, i.e. a slight decrease of the depth (not visible in figure). Since the wall growth rate is proportional to the depth perturbation, it turns out that this mechanism is stabilizing. Recalling again the vorticity equation, we can also show that the process is invariably stable, regardless of the wavenumber. In fact, for the W problem the boundary conditions read

$$\hat{\phi}(0) = -\hat{\phi}''(0) = \frac{2\chi\beta\Omega(\beta + \sinh\beta \cosh\beta)}{4\chi\beta^2(\beta \sinh\beta + \cosh\beta) + i\gamma\Omega(\sinh 2\beta - 2\beta)}, \quad (5.3)$$

$$\hat{\phi}(1) = 0. \quad (5.4)$$

Since γ is large and β small, the β^2 term of the denominator of the right-hand side of (5.3) is negligible and $\hat{\phi}(0)$ turns out to be almost independent of Ω . Therefore, the flow invariably displays two vortices rotating clockwise and anticlockwise in the positive and negative half-planes, respectively, as depicted in figure 9(c), regardless of the wavenumber. This means that the system is invariably stable. As announced, the fixed-bed problem has been shown to be unstable when $\Omega < 0$, while the W problem is always stable.

Let us move to the second issue: the relationship between parallel and non-parallel theories. At the end of § 4.2, we mentioned a possible scenario with a continuous transition from the wavelength selected at $\theta = 0$, as accounted for by the non-parallel theory, to the one provided on the flat part of the surface (far from the vertical region of the wall, i.e. $\theta \rightarrow \vartheta$), as accounted for by the parallel theory. It should be pointed out that a formal and quantitative description of this kind of continuation between the two theories is beyond the validity of the global-mode solution that we have presented, since that solution only holds very close to verticality. A possible way to circumvent the issue mathematically would be a three-deck theory that accounts for an intermediate layer that asymptotically matches both the upstream (curved) layer and the downstream (flat) layer.

However, there is a case that deserves to be investigated parametrically, wherein the two theories match naturally, namely when $\tilde{L}_y^H = \tilde{L}_y^G$. If (3.27) and (4.42) are used, the latter condition yields

$$\csc \vartheta = \Lambda(T) Re^{1/3} \tilde{\mathcal{R}}, \quad (5.5)$$

where the coefficient $\Lambda(T)$ ranges in the interval [0.77–1] for $T = [15-0]^\circ\text{C}$. The slopes of the flat region resulting from (5.5) are reported in figure 10 for different parametric conditions. It is worth noting that the reported values of ϑ span a reasonable interval for a realistic set of Re , $\tilde{\mathcal{R}}$ and T . Even though it is not rigorous, a potentially interesting pattern-based palaeo-flow reconstruction could be obtained using

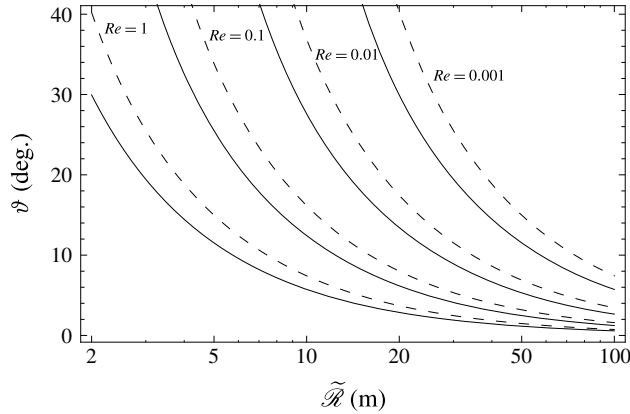


FIGURE 10. Relationship between the slope, Reynolds number and radius of curvature when parallel and non-parallel theories match naturally: $T = 0^{\circ}\text{C}$ (dashed lines); $T = 15^{\circ}\text{C}$ (solid lines).

this chart, by deducing the value of Reynolds number of the water film from simple geomorphic data such as ϑ and $\tilde{\mathcal{R}}$. On the contrary, the temperature is noticeably less important. This approach is limited to the particular case considered, which imposes the equality between the wavelengths selected between the two theories, a particular condition that must be visually checked in advance.

6. Concluding remarks

Elongated organ-pipe morphologies are widespread in ice and karst environments. The former case is very common over icefalls, the latter case bedecks the cave walls, wherein speleothems represent an important source of palaeo-climatic data. A novel approach relating fluid mechanics to the morphogenesis of such structures could therefore be of paramount importance. Through a unified modelling approach, we have solved the morphodynamic problem in terms of a stability analysis, and the typical features of karst and ice flutings have been shown to be hydrodynamically locked. The results obtained reject Squire's theorem when the Reynolds number is below a critical value that depends on the slope. The correct identification of the transition between flutings and ripples has been possible thanks to the numerical solution of the complete Orr–Sommerfeld-like problem, through an advanced spectral Galerkin technique.

Although the occurrence of the HLM is not essential to the instability discussed here, it has allowed us to explain that the morphogenesis of such patterns is completely driven by hydrodynamics. Note that the HLM would be a trivial finding if (2.3) was replaced by an algebraic relationship. The result is instead counterintuitive because the presence of a phenomenological evolution equation is expected to introduce new dynamics into the system, as in the case of ice ripples and crenulations (Camporeale & Ridolfi 2012a,b). Differently, in the present case, it appears that the wall dynamics of fluted patterns (which occur at inverted conditions) are fully slaved to hydrodynamics in a very wide range of the morphological parameter γ , thus embedding completely different environmental conditions, such as icefall and caves.

Another advantage in demonstrating the HLM comes from adopting the framework of the hydrodynamic stability analysis for Stokes flow. Indeed, parallel and non-

parallel stability analyses of inverted creeping flows have provided several analytical results about the selected wavelength, which match well with observations. The parallel theory readily provides the wavelengths at various slopes, but fails close to verticality. The non-parallel theory gives a local result only in a neighbourhood of verticality.

It is worth noting that in the parallel case there is no dependence of flute spacing on Reynolds number; instead it appears as a result of the non-parallel theory, namely at the head of flutes, through a one-sixth power law. Such a dependence of pattern wavelength on flow characteristics could be of palaeo-climatic interest. Nowadays, karst environments are in fact acquiring relevance in the field of palaeo-climate reconstructions. Several pieces of research have demonstrated that mineral deposits constituting speleothems can record past climatic conditions: measurable properties of the speleothems (e.g. mineral composition, calcite crystals) can in fact be related to dripping water and to the surrounding environmental conditions in which the deposition occurred (McDermott, Matthey & Hawkesworth 2001). However, as pointed out by Fairchild *et al.* (2006), speleothem records cannot yet be given a unique climatological meaning.

The analytical theories provided in this work are limited to Stokes flows, namely when the Reynolds number is much smaller than unity, which is the norm for the phenomena herein investigated. Although an improvement to larger values of Re could be desirable, it is instructive to show that formula (4.42) is quite robust nevertheless. A suggestive example is provided by figure 1(g): a close observation of the fountain's features allows one to assume $\mathcal{R} \sim 0.2$ m, while the mean annual temperature is $T = 15^\circ\text{C}$. The evaluation of a precise value of the Reynolds number is prohibitive, so it is reasonable to assume a conservative range of potential values such as $Re = [20-500]$. With this setting, formula (4.42) returns $L_y^{(G)} = [5-8.5]$ cm, which is fairly close to the actual value, despite the fact that the Stokes approximation would be no longer valid at such conditions.

More generally, other boundary value problems involving interface dynamics that follow (2.3) should support the same results (e.g. photosynthetic biofilms), as long as the linear theory is valid. Nonlinearities can contribute to modify the final picture, possibly introducing pattern coarse-graining. We have neglected front dynamics, since the related fingering instability develops with time scales too short to have a morphological significance in the present context, as is evident from numerical simulations (Lin, Kondic & Filippov 2012).

Acknowledgements

I gratefully acknowledge the support of L. Ridolfi for his friendship and fruitful discussions, and the three anonymous reviewers for their constructive and valuable comments that have helped to improve the quality of the paper.

REFERENCES

- BATCHELOR, G. K. 1967 *An Introduction to Fluid Dynamics*. Cambridge University Press.
- BENNEY, B. J. 1966 Long waves in liquid films. *J. Math. Phys.* **45**, 150–155.
- BREUDO, L., LAURE, P., DIAS, F. & BRIDGES, T. J. 1999 Linear pulse structure and signalling in a film flow on an inclined plane. *J. Fluid Mech.* **396**, 37–71.
- CAMPORALE, C., CANUTO, C. & RIDOLFI, L. 2012 A spectral approach for the stability analysis of turbulent open-channel flows over granular beds. *Theor. Comput. Fluid Dyn.* **26** (1–4), 51–80.

- CAMPOREALE, C. & RIDOLFI, L. 2012a Hydrodynamic-driven stability analysis of morphological patterns on stalactites and implications for cave paleoflow reconstructions. *Phys. Rev. Lett.* **108**, 238501.
- CAMPOREALE, C. & RIDOLFI, L. 2012b Ice ripple formation at large Reynolds numbers. *J. Fluid Mech.* **694**, 225–251.
- CHAN, P. Y. & GOLDENFELD, N. 2007 Steady states and linear stability analysis of precipitation pattern formation at geothermal hot springs. *Phys. Rev. E* **76**, 046104.
- CHANG, H.-C. & DEMEKHIN, E. A. 2002 *Complex Wave Dynamics on Thin Films*. Elsevier.
- CHARRU, F. 2001 *Hydrodynamic Instabilities*. Cambridge University Press.
- CHEN, A. S.-H. 2014 Experiments on the growth and form of icicles. PhD thesis, University of Toronto.
- CHEN, A. S.-H. & MORRIS, S. W. 2013 On the origin and evolution of icicle ripples. *New J. Phys.* **15** (103012), 248–252.
- CHENG, M. & CHANG, H.-C. 1992 Subharmonic instabilities of finite amplitude monochromatic waves. *Phys. Fluids* **4**, 505–523.
- CHU, K. J. & DUKLER, A. E. 1974 Statistical characteristics of thin, wavy films: part 2. Studies of substrate and its wave structure. *AIChE J.* **20** (4), 695–706.
- CRASTER, R. V. & MATAR, O. K. 2009 Dynamics and stability of thin liquid films. *Rev. Mod. Phys.* **81**, 1131–1196.
- DEBRUIN, G. J. 1974 Stability of a layer of liquid flowing down an inclined plane. *J. Engng Maths* **8** (3), 259–270.
- DRESSLER, R. F. 1978 New nonlinear shallow-flow equations with curvature. *J. Hydraul Res.* **16** (3), 205–222.
- DREYBRODT, W. 1988 *Processes in Karst Systems*. Springer.
- DREYBRODT, W. & BUHMANN, D. 1991 A mass-transfer model for dissolution and precipitation of calcite from solutions in turbulent motion. *Chem. Geol.* **90** (1–2), 107–122.
- FAIRCHILD, I. J., SMITH, C. L., BAKER, A., FULLER, L., SPOTL, C., MATTEY, D., McDERMOTT, F. & E.I.M.P 2006 Modification and preservation of environmental signals in speleothems. *Earth-Sci. Rev.* **75**, 105–153.
- FLORYAN, J. M., DAVIS, S. H. & KELLY, R. E. 1987 Instabilities of a liquid-film flowing down a slightly inclined plane. *Phys. Fluids* **30** (4), 983–989.
- HAMMER, O., DYSTHE, D. K., LELU, B., LUND, H., MEAKIN, P. & JAMTVEIT, B. 2008 Calcite precipitation instability under laminar, open-channel flow. *Geochim. Cosmochim. Acta* **72** (20), 5009–5021.
- HUERRE, P. & ROSSI, M. 1998 Hydrodynamic instabilities in open flows. In *Hydrodynamics and Nonlinear Instabilities* (ed. C. Godreche & P. Manneville), pp. 81–294. Cambridge University Press.
- HUTTER, K. 1983 *Theoretical Glaciology*. Kluwer.
- KALLIADASIS, S., RUYER-QUIL, C., SCHEID, B. & VELARDE, M. G. 2012 *Falling Liquid Films*, Applied Mathematical Sciences, vol 176, p. 440. Springer; ISBN: 978-1-84882-366-2.
- KAPITSA, P. L. & KAPITSA, S. P. 1949 Wave flow of thin liquid layers. *Zh. Eksp. Teor. Fiz.* **19**, 105–120.
- KAUFMANN, G. 2003 Stalagmite growth and palaeo-climate: the numerical perspective. *Earth Planet. Sci. Lett.* **214** (1–2), 251–266.
- KAUFMANN, G. & DREYBRODT, W. 2007 Calcite dissolution kinetics in the system $\text{CaCO}_3\text{-H}_2\text{O-CO}_2$ at high undersaturation. *Geochim. Cosmochim. Acta* **71** (6), 1398–1410.
- LIN, T.-S., KONDIC, L. & FILIPPOV, A. 2012 Thin films flowing down inverted substrates: three-dimensional flow. *Phys. Fluids* **24** (022105), 1–17.
- LUO, H. & POZRIKIDIS, C. 2006 Effect of inertia on film flow over oblique and three-dimensional corrugations. *Phys. Fluids* **18**, 078107.
- MARTIN-PEREZ, A., MARTIN-GARCIA, R. & ALONSO-ZARZA, A. M. 2012 Diagenesis of a drapery speleothem from castanar cave: from dissolution to dolomitization. *Int. J. Speleo.* **41** (2), 251–266.

- MCDERMOTT, F., MATTEY, D. P. & HAWKESWORTH, C. 2001 Centennial-scale holocene climate variability revealed by a high-resolution speleothem delta O-18 record from SW Ireland. *Science* **294** (5545), 1328–1331.
- MEAKIN, P. & JAMTVEIT, B. 2010 Geological pattern formation by growth and dissolution in aqueous systems. *Proc. R. Soc. Lond. A* **466** (2115), 659–694.
- NUSSELT, W. 1916 The surface condensation of water vapour. *Z. Verein. Deutsch. Ing.* **60**, 541–546.
- PIERSON, F. W. & WHITAKER, S. 1977 Some theoretical and experimental observations of the wave structure of falling liquid films. *Ind. Engng Chem. Fundam.* **16**, 401–408.
- PRADAS, M., TSELUIKO, D. & KALLIADASIS, S. 2011 Rigorous coherent-structure theory for falling liquid films: viscous dispersion effects on bound-state formation and self-organization. *Phys. Fluids* **23** (4), 044104.
- RUYER-QUIL, C. & MANNEVILLE, P. 2000 Improved modeling of flows down inclined planes. *Eur. Phys. J. B* **15** (2), 357–369.
- SCHMID, P. J. & HENNINGSON, D. S. 2001 *Stability and Transition in Shear Flows*, 1st edn. Springer.
- SHEN, J. 1994 Efficient spectral-Galerkin methods I. Direct solvers for the second and fourth order equations using Legendre polynomials. *SIAM J. Sci. Comput.* **15** (6), 1489–1505.
- SHORT, M. B., BAYGENTS, J. C., BECK, J. W., STONE, D. A., TOOMEY, R. S. & GOLDSTEIN, R. E. 2005a Stalactite growth as a free-boundary problem: a geometric law and its platonic ideal. *Phys. Rev. Lett.* **94** (1), 018501.
- SHORT, M. B., BAYGENTS, J. C. & GOLDSTEIN, R. E. 2005b Stalactite growth as a free-boundary problem. *Phys. Fluids* **17** (8), 083101.
- SIVASHINSKY, G. I. & MICHELSON, D. M. 1980 On irregular wavy flow of a liquid-film down a vertical plane. *Progr. Theoret. Phys.* **63** (6), 2112–2114.
- TRAN-CONG, T. & BLAKE, J. R. 1982 General solutions of the Stokes' flow equations. *J. Math. Anal. Applics.* **90**, 72–84.
- UENO, K., FARZANEH, M., YAMAGUCHI, S. & TSUJI, H. 2010 Numerical and experimental verification of a theoretical model of ripple formation in ice growth under supercooled water film flow. *Fluid Dyn. Res.* **42** (2), 025508.
- VESIPA, R., CAMPOREALE, C. & RIDOLFI, L. 2015 Thin-film induced morphological instabilities over calcite surfaces. *Proc. R. Soc. Lond. A* **471**, 20150031.
- WANG, C. Y. 1981 Liquid film flowing slowly down a wavy incline. *AIChE J.* **27** (2), 207–212.
- WIERSCHEM, A., BONTOZOGLOU, V., HEINING, C., UECKER, H. & AKSEL, N. 2008 Linear resonance in viscous films on inclined wavy planes. *Intl J. Multiphase Flow* **34**, 580–589.
- WOODING, R. A. 1991 Growth of natural dams by deposition from steady supersaturated shallow flow. *J. Geophys. Res.* **96** (B1), 667–682.
- YIH, C. S. 1955 Stability of two-dimensional parallel flows for three-dimensional disturbances. *Q. Appl. Maths* **12**, 434–435.
- YIH, C. S. 1963 Stability of liquid flow down an inclined plane. *Phys. Fluids* **6**, 321–334.